

Moving mesh FSI approach for VIV simulation based on DG method with AMR technique

Jia-Jun Zou, Yun-Long Liu, Qi Kong, and A-Man Zhang

College of Shipbuilding Engineering, Harbin Engineering University, Harbin 150001, China

(*Electronic mail: yunlong_liu@hrbeu.edu.cn)

(Dated: 4 April 2025)

Vortex-induced vibration (VIV) remains a fundamental yet computationally challenging problem in computational fluid dynamics (CFD). This study develops a moving mesh Fluid-structure interaction (FSI) approach within a Runge-Kutta Discontinuous Galerkin (RKDG) adaptive mesh refinement (AMR) framework. The viscous term in the compressible Navier-Stokes (NS) equations is discretized using the high-order Interior Penalty Discontinuous Galerkin (IPDG) method. In addition to the above, key numerical advancements encompass the rigorous derivation of the Lax-Friedrichs (L-F) numerical flux formulation tailored for moving meshes, an enhanced AMR-driven nodal correction methodology designed for curved surface geometries, and the implementation of a ghost-node boundary condition treatment scheme to address dynamic mesh motion. Numerical validation proceeds through three phases: First, Couette flow simulations confirm the IPDG method's spatial convergence order. Subsequent analysis of unsteady flow past a cylinder demonstrate the AMR framework's efficacy in resolving vortex-dominated flow. Finally, six VIV benchmark cases are simulated using third-order IPDG discretization, establishing the proposed FSI approach's accuracy. Furthermore, synthetic jets (SJs) flow control is investigated through four frequency-variant SJs configurations. The results reveal that SJs can achieve completely VIV suppression at a low actuation frequency, while higher actuation frequencies reduce suppression efficiency due to the energy of the SJs is more in the form of acoustic wave.

I. INTRODUCTION

FSI phenomena are prevalent across diverse engineering disciplines, observed in physical systems ranging from submarine pipeline oscillations under hydrodynamic forces¹⁻³ to aeroelastic instabilities in aircraft structures⁴⁻⁶ and wind-induced vibrations in long-span bridge systems⁷⁻⁹. VIV serves as a paradigmatic FSI phenomenon, where transverse VIV has become a benchmark^{10,11} for validating FSI algorithms due to its geometrically simple configuration and rich phenomenological manifestations. This canonical problem is commonly investigated using an elastically mounted rigid cylinder model.

Extensive research has historically focused on advancing numerical simulations of VIV. Ahn and Kallinderis¹² employed the Arbitrary Lagrangian-Eulerian Finite Volume Method (ALE-FVM) coupled with an artificial compressibility approach in 2006 for VIV analysis. Subsequent developments include Xie et al.¹³ who investigated flexible cylindrical structures using FVM in 2012, and Han et al.¹⁴ who implemented the Immersed Boundary-Lattice Boltzmann Method (IB-LBM) in 2021 for VIV simulations. However, existing research predominantly remains confined to second-order accurate numerical schemes in FSI simulations. The potential of high-order accuracy methods, which exhibit superior numerical characteristics with reduced dispersion and dissipation, remains underexplored in FSI simulations. These high-order accuracy methods enable finer resolution of flow field structures under same grid compared to conventional second-order accuracy approaches such as second-order FVM. Building upon these foundations, this study proposes a high-order accuracy FSI approach based on the RKDG¹⁵⁻¹⁷ AMR framework.

The DG method, a prominent high-order finite element ap-

proach, features a compact scheme that facilitates AMR and parallel computing. When applying DG methods to NS equations, researchers have developed distinct discretization approaches for viscous terms, including: the Bassi-Rebay 1^{18,19} (BR1), Bassi-Rebay 2^{20,21} (BR2), IPDG²²⁻²⁴, Local DG²⁵⁻²⁷ (LDG), Compact DG^{28,29} (CDG), and Direct DG³⁰⁻³² (DDG). Among these variants, the IPDG method demonstrates superior computational efficiency and implementation simplicity. Consequently, this study adopts the IPDG method for discretizing the viscous terms of NS equations.

Although the DG method exhibits significant advantages in high-order accuracy, its computational efficiency remains constrained by considerable computational costs. It is noteworthy that the compact stencil characteristic of DG schemes makes them particularly suitable for integration with h-adaptive mesh refinement techniques³³⁻³⁶. This approach selectively refines or coarsens grid elements based on characteristic physical quantities within cells, such as velocity divergence or vorticity magnitude. By dynamically adapting the mesh resolution, this strategy achieves an optimal balance between computational accuracy and efficiency, enabling precise capture of critical flow features like shock waves and vortex cores while substantially reducing computational resource requirements.

Within the algorithmic theoretical framework, this study methodically constructs a computational architecture for solving compressible NS equations on moving mesh (Sec.II A). The theoretical development commences with spatial discretization employing the high-order IPDG method under the RKDG AMR framework (Sec.II B). Subsequently, a rigorous mathematical derivation of the L-F numerical flux³⁷ formulation specifically adapted for moving mesh systems is presented (Sec.II C). An enhanced AMR-driven nodal correction methodology is further proposed to address curved boundary

geometries with increased precision (Sec.IID). The implementation incorporates a ghost-node methodology for moving boundary condition enforcement in moving mesh configurations (Sec.IIE). The FSI computational protocol for VIV is systematically formulated (Sec.IIF), incorporating a third-order Total Variation Diminishing Runge-Kutta (TVD-RK) temporal integration scheme to ensure enhanced numerical stability during coupled system evolution.

The numerical validation section follows a systematic verification protocol. Initially, the IPDG method is implemented on fixed grids to solve the NS equations, with the classical Couette flow benchmark rigorously validating the high precision and computational reliability of the developed solver (Sec.III A). Subsequent analysis of unsteady flow past a cylinder demonstrate the AMR framework's efficacy in resolving vortex-dominated flow (Sec.III B). To further evaluate the approach's engineering applicability, six VIV benchmark cases are simulated using third-order IPDG discretization. Quantitative comparisons with authoritative literature data confirm the excellent computational accuracy and engineering robustness of the proposed moving mesh FSI approach. Ultimately, SJs flow control³⁸ is investigated through four frequency-variant SJs configurations, which not only substantiate the jet control strategy as a stable and efficient solution for VIV suppression, but more importantly unravel the intrinsic correlation between jet actuation frequency and vibration mitigation effectiveness (Sec.III C).

II. NUMERICAL METHODS AND TECHNIQUES

A. Fluid dynamics equations in a moving mesh

In the present VIV simulation, two distinct reference frames are employed: a stationary earth-fixed reference frame and a moving reference frame that moves synchronously with the rigid cylindrical structure. Within the RKDG AMR framework, this study develops a moving mesh FSI approach. Built upon the compressible NS equations, the work theoretically derives generalized hydrodynamic equations in the Eulerian reference frame that govern fluid motion within dynamically moving mesh. A distinguishing feature of these governing equations is the incorporation of an additional transport term originating from moving mesh, which constitutes a theoretical extension beyond the classical compressible NS equations and substantially enhances the approach's capability in modeling dynamic boundary problems.

In the Cartesian coordinate system, the two-dimensional compressible Navier-Stokes equations neglecting body forces and volumetric heat sources are presented as follows:

$$\frac{\partial \mathbf{U}}{\partial t} + \nabla \cdot (\mathbf{F}^c(\mathbf{U}) - \mathbf{F}^v(\mathbf{U}, \nabla \mathbf{U})) = 0, \quad (1)$$

where \mathbf{U} denotes the conserved variables, $\mathbf{F}^c = (\mathbf{F}_x^c, \mathbf{F}_y^c)$ represents the convective flux, and $\mathbf{F}^v = (\mathbf{F}_x^v, \mathbf{F}_y^v)$ corresponds to the viscous flux. Their specific forms are defined as follows:

$$\mathbf{U} = \begin{bmatrix} \rho \\ \rho u \\ \rho v \\ \rho E \end{bmatrix}, \mathbf{F}_x^c = \begin{bmatrix} \rho u \\ \rho u^2 + p \\ \rho uv \\ u(\rho E + p) \end{bmatrix}, \mathbf{F}_y^c = \begin{bmatrix} \rho v \\ \rho uv \\ \rho v^2 + p \\ v(\rho E + p) \end{bmatrix},$$

$$\mathbf{F}_x^v = \begin{bmatrix} 0 \\ \tau_{xx} \\ \tau_{xy} \\ u\tau_{xx} + v\tau_{xy} + k_c \frac{\partial T}{\partial x} \end{bmatrix}, \mathbf{F}_y^v = \begin{bmatrix} 0 \\ \tau_{yx} \\ \tau_{yy} \\ u\tau_{yx} + v\tau_{yy} + k_c \frac{\partial T}{\partial y} \end{bmatrix}, \quad (2)$$

where ρ , $\mathbf{V} = (u, v)$, p , E , and T denote the density, the velocity vector, the pressure, the specific total energy, and the temperature, respectively. Moreover, k_c is the thermal conductivity coefficient. For the Newtonian fluid, the viscous stress tensor is given by:

$$\boldsymbol{\tau} = \mu \left[\nabla \mathbf{V} + (\nabla \mathbf{V})^T - \frac{2}{3} (\nabla \cdot \mathbf{V}) \mathbf{I} \right], \quad (3)$$

where \mathbf{I} is the identity matrix, μ is the dynamic viscous coefficient. Since the specific internal energy e (per unit mass) and temperature T satisfy $e = C_v T$, we have:

$$k_c T = \frac{\mu \gamma}{\text{Pr}} e, \quad (4)$$

where γ is the ratio of the specific heats, Pr is the Prandtl number of the fluid (for air, the laminar Prandtl number is taken as 0.72). The total energy per unit mass E of the fluid can be expressed as:

$$E = \frac{|\mathbf{V}|^2}{2} + e. \quad (5)$$

For compressible fluids, the Tammann equation of state³⁹ (eos) is introduced to describe the relationship between the internal energy and pressure of the fluid:

$$p = \rho e(\gamma - 1) - \gamma P_w, \quad (6)$$

where P_w is the reference pressure of the fluid. In the test cases, the fluid is assumed to be an ideal gas, i. e. , $\gamma = 1.4$ and $P_w = 0$.

Ahn and Kallinderis¹² (2006) implemented VIV simulations using a moving reference frame in their ALE-FVM approach, where the coordinate system was attached to moving boundaries. In contrast, our methodology employs a stationary earth-fixed reference frame. The computational grid moves synchronously with the rigid cylindrical structure in translational motion, maintaining velocity consistency $\mathbf{V}_s = \mathbf{V}_{mesh} = (u_{mesh}, v_{mesh})$. Based on Eq. (1), the modified governing equations for fluid dynamics in this translational moving mesh system can be expressed as:

$$\frac{\partial^* \mathbf{U}}{\partial^* t} + \nabla \cdot (\mathbf{F}^c(\mathbf{U}) - \mathbf{F}^v(\mathbf{U}, \nabla \mathbf{U})) = \mathbf{V}_{mesh} \cdot \nabla \mathbf{U}, \quad (7)$$

The fundamental relationship between $\frac{\partial^* \mathbf{U}}{\partial^* t}$ and $\frac{\partial \mathbf{U}}{\partial t}$ defined as $\frac{\partial^* \mathbf{U}}{\partial^* t} = \frac{\partial \mathbf{U}}{\partial t} + \mathbf{V}_{mesh} \cdot \nabla \mathbf{U}$. The term $\mathbf{V}_{mesh} \cdot \nabla \mathbf{U}$ on the right-hand side physically represents the additional transport term

induced by the mesh motion. Consequently, Eq. (7) can be simplified to:

$$\frac{\partial^* \mathbf{U}}{\partial^* t} + \nabla \cdot (\mathbf{F}^c(\mathbf{U}) - \mathbf{F}^v(\mathbf{U}, \nabla \mathbf{U})) = -\mathbf{U} \nabla \cdot \mathbf{V}_{mesh}, \quad (8)$$

the new convective flux term is formally defined as:

$$\begin{aligned} \mathbf{F}^c(\mathbf{U}) &= (\mathbf{F}_x^c(\mathbf{U}), \mathbf{F}_y^c(\mathbf{U})) \\ &= (\mathbf{F}_x^c(\mathbf{U}) - u_{mesh} \mathbf{U}, \mathbf{F}_y^c(\mathbf{U}) - v_{mesh} \mathbf{U}). \end{aligned} \quad (9)$$

B. Review of the RKDG method

The RKDG method refers to a numerical discretization approach where temporal discretization is implemented using the TVD-Runge-Kutta scheme, while spatial discretization employs the DG method, thereby achieving spatiotemporal discretization of partial differential equations. Due to the high-order accuracy and inherent stability characteristics of the RKDG framework, we select this computational paradigm to solve Eq. (8).

Following the fundamental principles of the DG finite element framework, we seek the projection \mathbf{U}_h of the true unknown solution \mathbf{U} within the discontinuous finite element space over the computational domain. Let Ω denote the fluid domain with boundary $\partial\Omega$. The domain Ω is discretized into non-overlapping elements Ω_e , where each element boundary $\partial\Omega_e$ is associated with a unit outward normal vector $\mathbf{n} = (n_x, n_y)$. Following the aforementioned framework, we formally introduce the DG finite element space V_h , defined as:

$$V_h = \{ \varphi_h \in L^2(\Omega) : \varphi_h|_{\Omega_e} \in P^s(\Omega_e), \forall \Omega_e \in \Omega \}, \quad (10)$$

where $P^s(\Omega_e)$ denotes the space of polynomial functions of degree s on each element Ω_e . Within the DG framework, we first construct a set of basis functions $\{\varphi_i\}_{i=1}^N$ defined on the polynomial space $P^s(\Omega_e)$, where the dimension N is determined by $N = \frac{1}{2}(s+1)(s+2)$. Following the DG discretization strategy, the numerical solution \mathbf{U}_h within each computational element is expressed as a linear combination of these basis functions: $\mathbf{U}_h(\mathbf{x}, t) = \sum_{i=1}^N \mathbf{k}_i(t) \varphi_i(\mathbf{x})$. This representation achieves spatiotemporal decoupling of the approximate solution, where the time-dependent coefficient vectors $\mathbf{k}_i(t)$ exclusively serve as the degrees of freedom (DOFs) within the local element. By applying the Galerkin integration procedure to Eq. (8) over an individual element:

$$\begin{aligned} & \int_{\Omega_e} \frac{\partial^* \mathbf{U}}{\partial^* t} \varphi_i dS \\ &= - \int_{\Omega_e} [\nabla \cdot (\mathbf{F}^c(\mathbf{U}) - \mathbf{F}^v(\mathbf{U}, \nabla \mathbf{U})) \varphi_i - \mathbf{U} \nabla \cdot \mathbf{V}_{mesh} \varphi_i] dS \\ &= \int_{\Omega_e} [(\mathbf{F}^c(\mathbf{U}) - \mathbf{F}^v(\mathbf{U}, \nabla \mathbf{U})) \cdot \nabla \varphi_i - \mathbf{U} \nabla \cdot \mathbf{V}_{mesh} \varphi_i] dS \\ & \quad - \int_{\partial\Omega_e} [(\hat{\mathbf{F}}^c(\mathbf{U}) - \hat{\mathbf{F}}^v(\mathbf{U}, \nabla \mathbf{U})) \cdot \mathbf{n} \varphi_i] dl, \end{aligned} \quad (11)$$

the terms $\hat{\mathbf{F}}^c(\mathbf{U}) \cdot \mathbf{n}$ and $\hat{\mathbf{F}}^v(\mathbf{U}, \nabla \mathbf{U}) \cdot \mathbf{n}$ represent the convective numerical flux and viscous numerical flux, respectively, at element boundaries.

To preserve flux conservation and scheme consistency, the convective numerical flux $\hat{\mathbf{F}}^c(\mathbf{U}) \cdot \mathbf{n}$ is constructed using an approximate Riemann solver. Given that all investigated cases involve low-Mach-number regimes without strong discontinuities, numerical experiments demonstrate negligible computational difference to the selection of different convective numerical flux schemes. For computational efficiency optimization, the Lax-Friedrichs numerical flux, characterized by its lower computational overhead, is ultimately adopted, while the viscous numerical flux $\hat{\mathbf{F}}^v(\mathbf{U}, \nabla \mathbf{U}) \cdot \mathbf{n}$ adopts the IPDG numerical flux. The detailed implementation procedures for these numerical fluxes are comprehensively described in Section II C.

Substituting the numerical solution $\mathbf{U}_h(\mathbf{x}, t)$ into Eq. (11), and considering all test functions $\{\varphi_i\}_{i=1}^N$, each element generates a linear system of the form:

$$\mathbf{M} \dot{\mathbf{K}} = \mathbf{R}, \quad (12)$$

where \mathbf{M} is the $N \times N$ mass matrix, $\dot{\mathbf{K}}$ denotes the time derivative of the coefficient matrix, \mathbf{R} is the right-hand side matrix.

The temporal discretization employs the third-order TVD-Runge-Kutta method⁴⁰ as detailed in Eq. (28). The expression for the time step Δt adopted in this paper is given by:

$$\Delta t = \frac{q}{\frac{\sqrt{u^2 + v^2 + c_s}}{h} + \frac{\mu}{\rho h^2}}, \quad (13)$$

in which q is the Courant-Friedrichs-Lewy number, h is the mesh size, c_s denotes the speed of sound.

The RKDG computational framework has thus been established now. During RKDG simulations, numerical oscillations arise when flow discontinuities propagate into computational cell interiors. Such oscillations may erroneously render inherently positive-definite physical quantities (e.g., density and pressure) negative, thereby destabilizing the computational process. To address this challenge, researchers have developed various shock-capturing approaches, primarily categorized into artificial viscosity methods, reconstruction-based methods, and limiter techniques. Artificial viscosity methods⁴¹, being the earliest proposed approach, suffer from significant parameter dependence and tend to introduce excessive numerical dissipation. Recently, Liu et al. developed an entropy-stable artificial viscosity method⁴². Reconstruction-based discontinuity-capturing methods⁴³ face implementation challenges in complex geometries and three-dimensional problems due to their non-compact stencil. In contrast, limiter techniques demonstrate superior flexibility in handling complex geometries and three-dimensional problems. Considering the physical discontinuities that emerge near jet orifices in VIV suppression simulations, this study employs a positivity-preserving limiter for strong shock capture within the RKDG framework, as proposed by Liu et al.¹⁶ in 2016, combined with an unstructured grid-adapted WENO limiter¹⁷ to ensure computational stability and accuracy.

C. numerical flux formulation for moving mesh

L-F numerical flux³⁷ formulation for moving mesh is given by:

$$\hat{\mathbf{F}}^{\tilde{c}}(\mathbf{U}^-, \mathbf{U}^+) \cdot \mathbf{n} = \frac{1}{2}((\mathbf{F}^{\tilde{c}}(\mathbf{U}^-) + \mathbf{F}^{\tilde{c}}(\mathbf{U}^+)) \cdot \mathbf{n} - \alpha(\mathbf{U}^+ - \mathbf{U}^-)), \quad (14)$$

where α is the maximum absolute value among all eigenvalues of both Jacobian matrices $\tilde{J}_+ = \frac{\partial \mathbf{F}^{\tilde{c}}(\mathbf{U}^+) \cdot \mathbf{n}}{\partial \mathbf{U}^+}$ and $\tilde{J}_- = \frac{\partial \mathbf{F}^{\tilde{c}}(\mathbf{U}^-) \cdot \mathbf{n}}{\partial \mathbf{U}^-}$. It is worth noting that, due to the relationship in Eq. (9), the Jacobian matrices $\tilde{J} = \frac{\partial \mathbf{F}^{\tilde{c}}(\mathbf{U}) \cdot \mathbf{n}}{\partial \mathbf{U}}$ and $J = \frac{\partial \mathbf{F}^c(\mathbf{U}) \cdot \mathbf{n}}{\partial \mathbf{U}}$ satisfy the following relationship:

$$\frac{\partial \mathbf{F}^{\tilde{c}}(\mathbf{U}) \cdot \mathbf{n}}{\partial \mathbf{U}} = \frac{\partial \mathbf{F}^c(\mathbf{U}) \cdot \mathbf{n}}{\partial \mathbf{U}} - (\mathbf{V}_{mesh} \cdot \mathbf{n})\mathbf{I}. \quad (15)$$

Furthermore, it can be shown that the Jacobian matrices $\tilde{J} = \frac{\partial \mathbf{F}^{\tilde{c}}(\mathbf{U}) \cdot \mathbf{n}}{\partial \mathbf{U}}$ and $J = \frac{\partial \mathbf{F}^c(\mathbf{U}) \cdot \mathbf{n}}{\partial \mathbf{U}}$ share the same right eigenvector matrix, and their diagonal eigenvalue matrices $\tilde{\lambda}$ (for $\frac{\partial \mathbf{F}^{\tilde{c}}(\mathbf{U}) \cdot \mathbf{n}}{\partial \mathbf{U}}$) and λ (for $\frac{\partial \mathbf{F}^c(\mathbf{U}) \cdot \mathbf{n}}{\partial \mathbf{U}}$) satisfy the following relationship:

$$\tilde{\lambda} = \lambda - (\mathbf{V}_{mesh} \cdot \mathbf{n})\mathbf{I}. \quad (16)$$

Therefore, the characteristic speed α is derived from the following formula: $\alpha = \max\{(|\mathbf{V} \cdot \mathbf{n} - \mathbf{V}_{mesh} \cdot \mathbf{n}| + c)^+, (|\mathbf{V} \cdot \mathbf{n} - \mathbf{V}_{mesh} \cdot \mathbf{n}| + c)^-\}$

The IPDG viscous numerical flux⁴⁴ enhances the weak continuity of the conservative vector at element interfaces by incorporating a penalty term, which is formulated as follows:

$$\hat{\mathbf{F}}^v(\mathbf{U}, \nabla \mathbf{U}) \cdot \mathbf{n} = \frac{\mathbf{F}^{v,+} + \mathbf{F}^{v,-}}{2} \cdot \mathbf{n} - C_{ip} \mu \frac{s^2}{h} (\mathbf{U}^- - \mathbf{U}^+), \quad (17)$$

in which C_{ip} is the penalty coefficient, typically chosen as a positive constant. It is worth noting that there is currently no universally optimal method for selecting C_{ip} . Appropriately increasing C_{ip} can enhance the continuity of the solution at element interfaces; however, excessively large values of C_{ip} may lead to an ill-conditioned problem. In this work, $C_{ip} = 4$.

D. AMR and an enhanced AMR-driven nodal correction methodology for curved surface geometries

This study employs the FSMESH module within the FSI software FSLAB⁴⁵ to implement dynamic adaptive mesh refinement (AMR) under large-scale MPI parallelization. The AMR framework utilizes a block-based quad-tree data structure, where each parent block splits into four child blocks during refinement and conversely merges from four child blocks during coarsening. Each block contains N_{seg}^2 computational cells, with explicit DG solutions computed at the individual cell level. Boundary data exchange between blocks is managed through direct communication with neighboring blocks. The AMR configuration specifies a user-defined minimum refinement level A_{min} and a user-defined maximum level A_{max} .

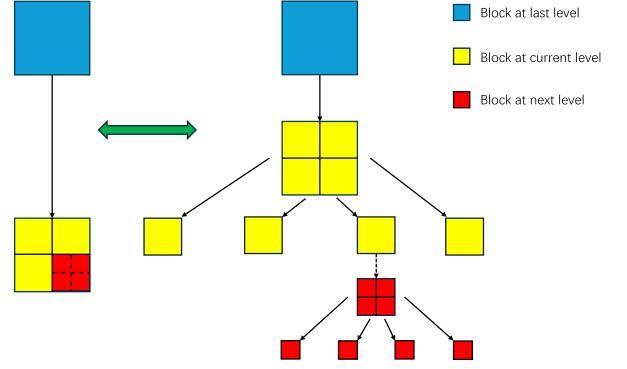


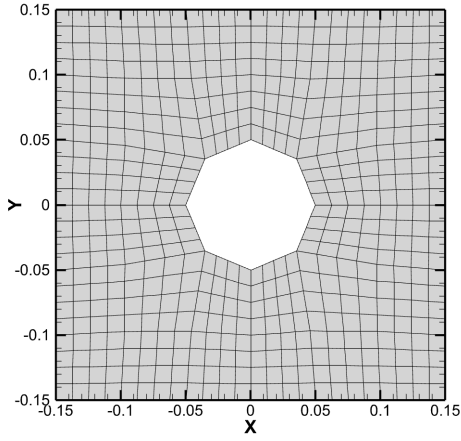
FIG. 1: Schematic of quad-tree AMR architecture.

Fig. 1 schematically illustrates this quad-tree AMR architecture.

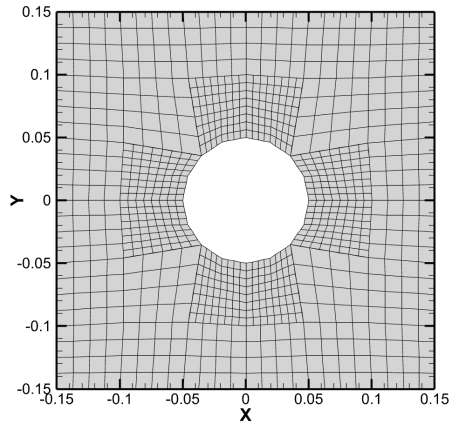
In the numerical examples presented in this study, a key objective is to establish an appropriate adaptive criterion for AMR in regions exhibiting vortex structures. To achieve this, we define a dimensionless vorticity parameter in the z -direction: $\omega_z^* = \frac{\omega_z d}{2|\mathbf{V}_\infty|}$, where ω_z represents the physical vorticity component in the z -direction, d denotes the cylinder diameter, and \mathbf{V}_∞ corresponds to the free-stream velocity. The adaptive strategy is implemented through two threshold values: ω_{min} and ω_{max} . Local mesh refinement is triggered when $\omega_z^* > \omega_{max}$, and mesh coarsening is applied when $\omega_z^* < \omega_{min}$. This dual-threshold approach ensures concentrated computational resolution in high-vorticity regions while maintaining efficiency through coarsening in low-vorticity regions.

The high-precision nature of DG methods presents a challenge in geometrically complex regions: excessively dense grids incur prohibitive computational costs, while overly coarse grids compromise boundary representation fidelity. To resolve this problem, Kong et al.⁴⁶ (2023) proposed an AMR-driven block node correction method for curved boundaries. This approach iteratively adjusts nodes of AMR blocks intersecting curved surfaces to progressively converge toward theoretical boundary profiles. Building upon this foundation, this study propose an enhanced cell node correction method that significantly improves the geometric approximation capability of quadrilateral elements for curved boundaries through AMR-driven refinement.

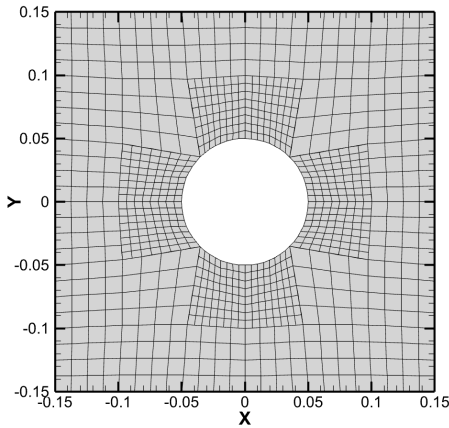
The block node correction method repositions nodes of all refined blocks adjacent to curved boundaries to their theoretical positions. Our cell node correction method extends this framework by further optimizing nodes of individual cells along block edges. As an illustrative example using a circular geometry with radius $R = 0.05$, Fig. 2 demonstrates the comparative corrective performance between the block-based nodal correction method proposed by Kong et al. and the cell-based method developed in this work.



(a) without correction



(b) with block-based correction



(c) with cell-based correction

FIG. 2: Comparison of block-based and cell-based nodal correction methods for curved boundaries.

E. Ghost-node boundary condition treatment for moving mesh

In CFD, appropriate boundary condition implementation constitutes a critical methodological consideration. Improper boundary treatments may induce significant computational errors or even divergence. To address this challenge, this study develops a moving boundary condition strategy through a two-tiered approach: 1) Domain Coupling: Establishes correspondence between external ghost points $(\cdot)_R$ and internal physical Gauss points $(\cdot)_L$. 2) ghost Gauss Point Extension: Prescribes values to an extended layer of ghost Gauss points beyond the computational domain boundary. All numerical integrations employ Gauss-Lobatto quadrature points (Fig. 3), selected for their enhanced numerical stability and spectral accuracy characteristics at domain boundaries. This section introduces three types of moving-wall boundary conditions implemented through the ghost node method:

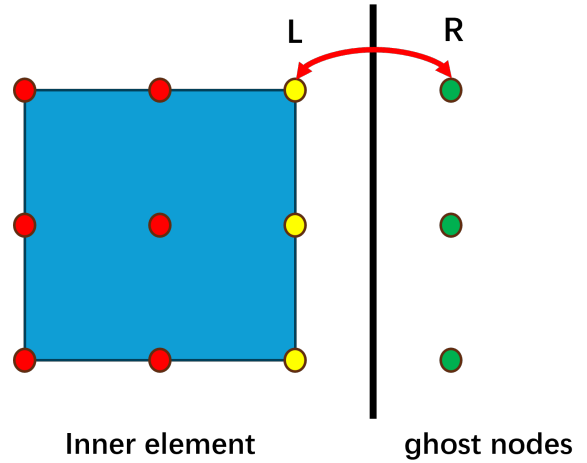


FIG. 3: Schematic of ghost-node boundary condition treatment.

(1) Adiabatic no-slip boundary condition for moving surfaces.

The fundamental mathematical formulation of the adiabatic no-slip boundary condition is expressed as:

$$\begin{aligned} \mathbf{V} &= \mathbf{V}_{wall} = \mathbf{V}_{mesh}, \\ \frac{\partial T}{\partial \mathbf{n}} &= 0. \end{aligned} \quad (18)$$

Following the principles of boundary layer theory, the following relationships can be derived:

$$\begin{aligned} p_R &= p_L, \\ T_R &= T_L, \\ e_R &= e_L, \\ \rho_R &= \rho_L, \\ \mathbf{V}_R &= -\mathbf{V}_L + 2\mathbf{V}_{mesh}. \end{aligned} \quad (19)$$

(2) Isothermal no-slip boundary condition for moving surfaces.

The isothermal no-slip boundary condition differs from the adiabatic no-slip condition in that the boundary temperature is explicitly prescribed as follows:

$$\begin{aligned}\mathbf{V} &= \mathbf{V}_{wall} = \mathbf{V}_{mesh}, \\ T &= T_{wall}.\end{aligned}\quad (20)$$

Following the principles of boundary layer theory and Tammann eos, the following relationships can be derived:

$$\begin{aligned}T_R &= T_{wall}, \\ e_R &= C_v T_R, \\ p_R &= p_L, \\ \rho_R &= \frac{p_R + \gamma P_w}{e_R(\gamma - 1)}, \\ \rho_L \mathbf{V}_L + \rho_R \mathbf{V}_R &= (\rho_L + \rho_R) \mathbf{V}_{mesh}.\end{aligned}\quad (21)$$

(3) Dynamic jet boundary condition.

When simulating jet flow for vortex-induced vibration suppression (see Section III C for details), dynamic jet boundary conditions must be imposed on the jet orifices:

$$\mathbf{V}_R = \mathbf{V}_{wall} + \mathbf{V}_{sj}.\quad (22)$$

F. Governing equation for the oscillating cylinder and computational methods for FSI

Using the transverse VIV of a circular cylinder as a benchmark case, we present the structural governing equations, moving mesh FSI computational framework, and FSI time-stepping scheme for FSI analysis. The structural governing equations for transverse VIV of a circular cylinder⁴⁷ can be formulated as:

$$m\ddot{y} + c\dot{y} + ky = F_l(t),\quad (23)$$

in which $F_l(t)$ denotes the time-varying lift acting on the cylinder, y represents the instantaneous position of the rigid cylinder, \dot{y} and \ddot{y} denote its velocity and acceleration, respectively. The parameters m , c and k correspond to the cylinder mass, structural damping coefficient, and stiffness coefficient. To nondimensionalize the structural governing Eq. (23), we introduce the following dimensionless variables and parameters:

$$\begin{aligned}Y &= \frac{y}{d}, T = \frac{t}{d/u_\infty}, \\ C_l &= \frac{2F_l}{\rho_\infty u_\infty^2 d}, C_d = \frac{2F_d}{\rho_\infty u_\infty^2 d}, St = \frac{f_v d}{u_\infty}, \\ m^* &= \frac{m}{\rho_\infty d^2}, c^* = \frac{c}{2\sqrt{km}}, \\ U_R &= \frac{u_\infty}{f_n d}, f_n = \frac{1}{2\pi} \sqrt{\frac{k}{m}}, \\ Re &= \frac{\rho_\infty u_\infty d}{\mu}, Ma = \frac{u_\infty}{c_\infty},\end{aligned}\quad (24)$$

where Y is the dimensionless displacement, and T is the dimensionless time. ρ_∞ denotes the free-stream fluid density, C_l

and C_d represent the lift and drag coefficients, respectively, f_v and St are the vortex shedding frequency and Strouhal number. The mass ratio m^* characterizes the hydrodynamic inertia of the cylinder, and c^* is the dimensionless damping coefficient. The reduced velocity U_R quantifies the stiffness of the structural system: larger U_R corresponds to smaller natural frequency f_n , indicating reduced structural stiffness. Here, f_n denotes the natural frequency of the structural system. Additionally, Re (Reynolds number) and Ma (Mach number) characterize the flow regime, and c_∞ is the local speed of sound in the free-stream fluid. The formulations for lift and drag calculations are given in Eq. (25):

$$\begin{aligned}F_d &= F_{dp} + F_{df} = \oint -pn_x dl + \oint \tau_{xx}n_x + \tau_{yx}n_y dl, \\ F_l &= F_{lp} + F_{lf} = \oint -pn_y dl + \oint \tau_{xy}n_x + \tau_{yy}n_y dl,\end{aligned}\quad (25)$$

here, $\mathbf{n} = (n_x, n_y)$ denotes the unit outward normal vector of the cylinder.

The structural governing Eq. (23) can be nondimensionalized to yield the following dimensionless form:

$$\frac{d^2 Y}{dT^2} + \left(\frac{4\pi c^*}{U_R}\right) \frac{dY}{dT} + \left(\frac{4\pi^2}{U_R^2}\right) Y = \frac{C_l}{2m^*}\quad (26)$$

The computational framework of the moving mesh FSI method for transverse VIV of a circular cylinder is illustrated in Fig. 4. The specific computational procedure is as follows:

1. **Initialization:** Assume the acceleration, velocity, and displacement of the cylinder at time t_n are known: \ddot{y}^n , \dot{y}^n , y^n .
2. **Time-Step Update:** Update the velocity and displacement at t_{n+1} using the values at t_n : \dot{y}^{n+1} , y^{n+1} .
3. **Fluid-Solid Coupling:**
 - Impose the mesh velocity $\mathbf{V}_{mesh} = (0, \dot{y}^n)$ into Eq. (8) to update the governing equations and cylinder boundary conditions.
 - Solve the flow field using the IPDG method to obtain the updated flow variables at t_{n+1} : $\mathbf{U}_{t_{n+1}}$.
 - Compute the lift at t_{n+1} : $F_l(\mathbf{U}_{t_{n+1}})$.
4. **Oscillating cylinder Dynamics:** Calculate the updated acceleration at t_{n+1} using Eq. (23): \ddot{y}^{n+1} .

Through this iterative process, the acceleration, velocity, and displacement at t_n —denoted as $\ddot{y}^n, \dot{y}^n, y^n$ —are advanced to t_{n+1} , yielding $\ddot{y}^{n+1}, \dot{y}^{n+1}, y^{n+1}$.

In the temporal advancement of the moving mesh FSI framework, this work employs a third-order TVD-Runge-Kutta method to concurrently advance both the fluid and structural subsystems. Let \mathbf{Z} denote the coupled fluid-structure state vector undergoing time integration, defined as:

$$\mathbf{Z} = \begin{bmatrix} \mathbf{U} \\ y \\ \dot{y} \end{bmatrix}\quad (27)$$

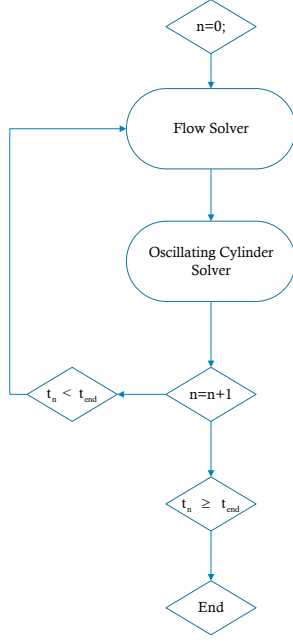


FIG. 4: Schematic of computational procedure for FSI.

The time advancement of the coupled fluid-structure state vector \mathbf{Z} is shown:

$$\begin{aligned}
 \mathbf{Z}^{(1)} &= \mathbf{Z}^{t_n} + \Delta t \dot{\mathbf{Z}}^{t_n} \\
 \ddot{\mathbf{y}}^{(1)} &= \left(F_l^{(1)} \left(\tilde{\mathbf{U}}^{(1)} \right) - c\dot{\mathbf{y}}^{(1)} - k\mathbf{y}^{(1)} \right) / m \\
 \mathbf{Z}^{(2)} &= \frac{3}{4} \mathbf{Z}^{t_n} + \frac{1}{4} \mathbf{Z}^{(1)} + \frac{1}{4} \Delta t \dot{\mathbf{Z}}^{(1)} \\
 \ddot{\mathbf{y}}^{(2)} &= \left(F_l^{(2)} \left(\tilde{\mathbf{U}}^{(2)} \right) - c\dot{\mathbf{y}}^{(2)} - k\mathbf{y}^{(2)} \right) / m \\
 \mathbf{Z}^{t_{n+1}} &= \frac{1}{3} \mathbf{Z}^{t_n} + \frac{2}{3} \mathbf{Z}^{(2)} + \frac{2}{3} \Delta t \dot{\mathbf{Z}}^{(2)} \\
 \ddot{\mathbf{y}}^{t_{n+1}} &= \left(F_l^{(3)} \left(\tilde{\mathbf{U}}^{(3)} \right) - c\dot{\mathbf{y}}^{t_{n+1}} - k\mathbf{y}^{t_{n+1}} \right) / m
 \end{aligned} \tag{28}$$

III. NUMERICAL VERIFICATION

A. Couette flow

When the mesh remains stationary ($\mathbf{V}_{mesh} \equiv \mathbf{0}$), Eq. (8) reduces to Eq. (1). The Couette flow, serving as an analytical solution to the compressible NS equations, is frequently employed to validate the order-of-accuracy of NS solvers. The physical configuration comprises viscous fluid motion between two parallel plates with the following boundary speci-

fications: the lower plate is fixed with constant temperature T_0 , the upper plate has a velocity V_1 with constant temperature T_1 , the gap height between the plates is H . Under constant dynamic viscosity μ , the analytical solution⁴⁸ for this problem is given by:

$$\begin{aligned}
 u &= \frac{V_1}{H} y, v = 0, \\
 T &= T_0 + \frac{T_1 - T_0}{H} y + \frac{\mu V_1^2}{2k} \cdot \frac{y}{H} \left(1 - \frac{y}{H} \right), \\
 p &= \text{constant}, \rho = \frac{p}{RT}.
 \end{aligned} \tag{29}$$

In this case, $V_1 = 1.0, H = 1.0, T_0 = 0.8, T_1 = 0.85, \mu = 0.01$. The L2-norm error convergence and accuracy of density computed by solving the NS equations using IPDG methods of different orders are summarized in Table I. Here, IP(2), IP(3), and IP(4) denote the Interior Penalty Discontinuous Galerkin schemes with second-order, third-order, and fourth-order accuracy, respectively.

As can be seen from Table I, even on the same 2×2 grid, as the IPDG order increases from 2 to 4, the error magnitude decreases from $1e-3$ to $1e-5$ and further to $1e-6$. This demonstrates that elevating the IPDG order can significantly improve the accuracy of flow field simulations, thereby validating the high-order accuracy characteristics of the solver developed in this study.

B. Flow over a cylinder

This section presents a two-dimensional unsteady simulation of cylinder flow. The cylinder diameter is set as $d = 0.1$. The freestream conditions are Mach number $Ma = 0.2$ and Reynolds number $Re = 150$. The computational domain spans $[-2.4, 4.4] \times [-2.4, 2.4]$ with the cylinder center located at $(0, 0)$. An adiabatic no-slip boundary condition is applied to the cylinder wall, where the cylindrical surface is constructed using the cell-based node correction method proposed in this study. Non-reflective boundary conditions⁴⁹ are implemented at all far-field boundaries. To demonstrate the superiority of the RKDG AMR framework, dynamic AMR technology is employed to capture vortex structures. The initial block partitioning of the computational domain and the local initial mesh near the cylinder are shown in Fig. 5 and Fig. 6, respectively.

In this section, numerical solutions of the compressible NS equations (where Eq. (8) reduces to the NS equations under stationary grid conditions) are obtained using the IP(2), IP(3), and IP(4) schemes, respectively. The integration domains for the pressure lift F_{lp} , viscous lift F_{lf} , pressure drag F_{dp} , and viscous drag F_{df} are all defined over the cylinder boundary. The computed lift coefficient, drag coefficient, and Strouhal number are compared against those reported by Zhang⁵⁰ and Müller et al.⁵¹, as summarized in Table II. The time evolution of the pressure lift and pressure drag coefficients computed by IP(4) are shown in Fig. 7. The time evolution of the viscous lift and viscous drag coefficients computed by IP(4) are shown in Fig. 8. The time evolution of the lift and drag coefficients computed by IP(4) are shown in Fig. 9.

TABLE I: Convergence and accuracy of density computed by solving the NS equations using IPDG methods of different orders.

grid	IP(2)		IP(3)		IP(4)	
	L2 error	Order	L2 error	Order	L2 error	Order
2×2	5.18e-3		6.8e-5		1.64e-6	
4×4	1.28e-3	2.0168	8.7e-6	2.9664	8.52e-8	4.2667
8×8	3.2e-4	2.00	1.02e-6	3.0924	4.35e-9	4.2918

TABLE II: Comparison of lift and drag coefficients and Strouhal numbers.

	Time-averaged C_d	ΔC_d peak to peak	ΔC_l peak to peak	Strouhal number
IP(2)	1.33	0.0497	1.016	0.187
IP(3)	1.3503	0.0518	1.04	0.1845
IP(4)	1.3547	0.0512	1.0456	0.1847
Zhang	1.348	0.0519	1.048	0.184
Müller	1.34	0.05228	1.0406	0.183

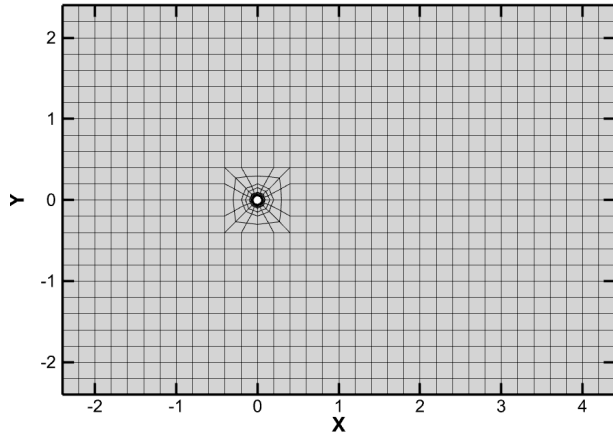


FIG. 5: The initial block partitioning of the computational domain.

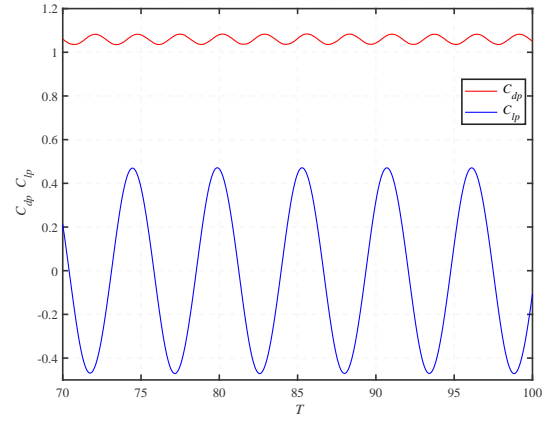


FIG. 7: The time evolution of the pressure lift and pressure drag coefficients computed by IP(4).

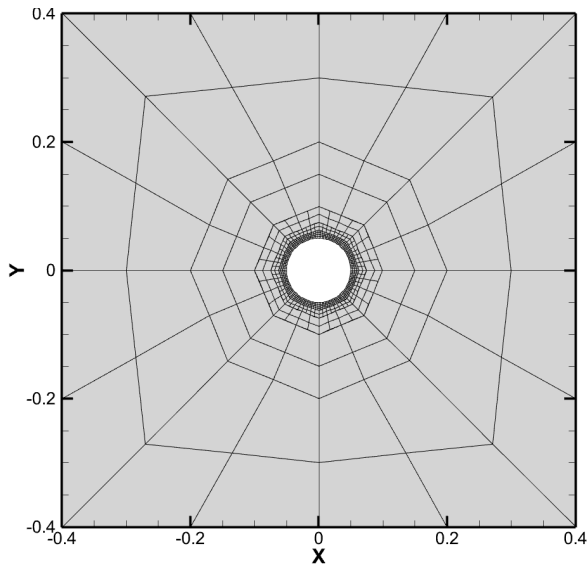


FIG. 6: The local initial mesh near the cylinder.

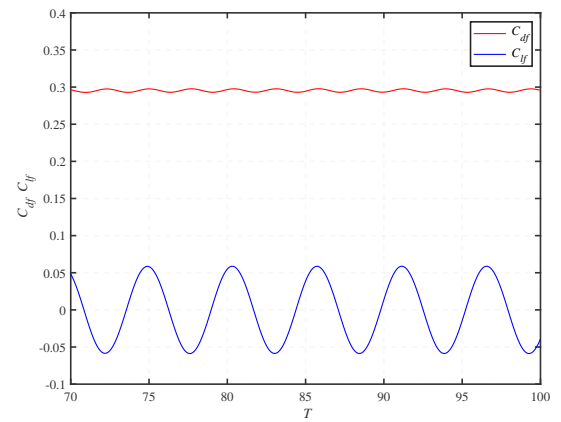


FIG. 8: The time evolution of the viscous lift and viscous drag coefficients computed by IP(4).

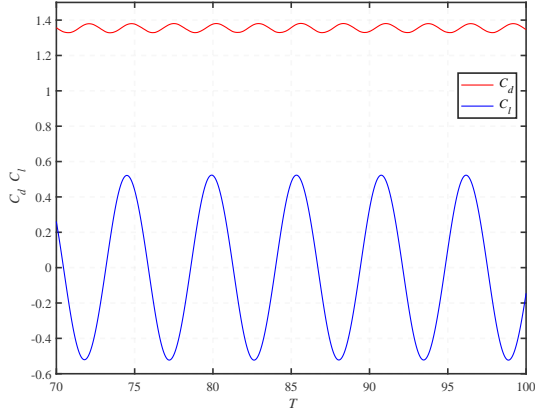


FIG. 9: The time evolution of the lift and drag coefficients computed by IP(4).

Figure 10 compares the dimensionless vorticity ω_z^* contours simulated using IP(2), IP(3), and IP(4) methods at an identical time instance $T=100$. The lower-order IP(2) scheme exhibits significant distortion in flow field evolution due to its reduced accuracy and amplified numerical dissipation. In contrast, the higher-order IP(3) and IP(4) formulations demonstrate remarkable convergence, with their vorticity patterns showing negligible differences.

As clearly shown in Fig. 10, the ω_z^* contour plots obtained with the IP(2) scheme exhibit relatively low resolution. However, when the solution accuracy is elevated to IP(3) and IP(4) levels, a significant enhancement in the resolution of ω_z^* contours is achieved, yielding high-fidelity flow field visualizations. This demonstrates that for the same coarse grid configuration, increasing the IPDG order can effectively improve solution precision, thereby fully validating the superior capability of high-order IPDG methods in resolving complex fluid dynamic phenomena.

The dimensionless vorticity ω_z^* contour plots and AMR block partitioning computed using the IP(4) method are shown in Figure 11. Figure 11 demonstrates that the blocks are dynamically refined to the maximum adaptive level A_{max} in regions with sufficiently large ω_z^* values, whereas grid is maintained in areas with diminished ω_z^* magnitudes. This adaptive refinement strategy achieves substantial computational efficiency gains while preserving solution accuracy, thereby validating the superior performance of the AMR technology used in this study.

C. Synthetic jets flow control for VIV

To balance computational accuracy and efficiency, the IP(3) scheme is employed to solve Eq. (8). Subsequently, six direct numerical simulations (DNS) of transverse VIV benchmark cases are simulated using IP(3) within the RKDG AMR framework, establishing the proposed FSI approach's accuracy. Furthermore, the FSI approach is employed to inves-

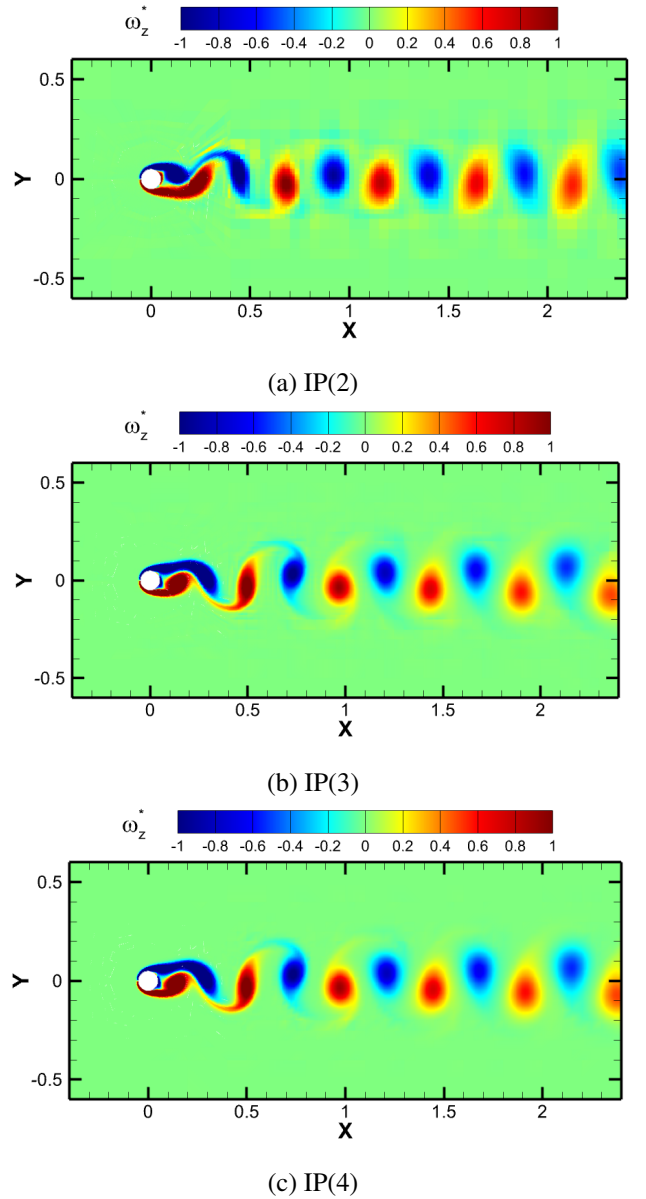


FIG. 10: The dimensionless vorticity ω_z^* contour plots computed using IP(2), IP(3), and IP(4) at $T=100$.

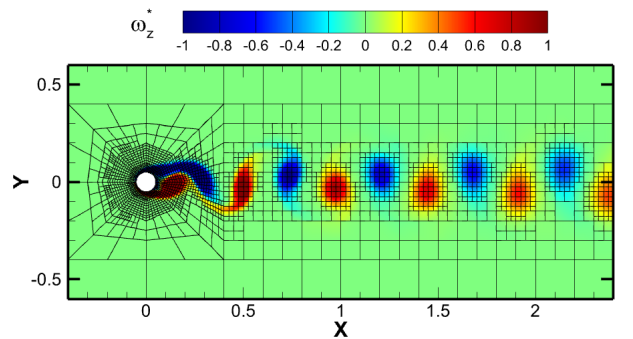


FIG. 11: The dimensionless vorticity ω_z^* contour plots and AMR block partitioning computed using IP(4).

tigate active flow control SJs for VIV suppression^{52–54}, with particular emphasis on the correlation between SJs actuation frequency and suppression performance.

All numerical cases in this section employ the identical computational domain as specified in Section III B, with the cylindrical boundary prescribed as a transient-moving adiabatic no-slip boundary condition. The parameters for the transverse VIV benchmark cases are set as:

$$\text{Re} = 150, \quad m^* = 2, \quad c^* = 0.0, \quad U_R = 3.0\text{--}8.0$$

with a Mach number $\text{Ma} = 0.085 < 0.2$, satisfying the incompressibility condition. The computed results of the maximum dimensionless displacement Y_{\max} are shown in Fig. 12.

Fig. 12 presents the scatter plot of vibration amplitude versus reduced velocity U_R for transverse VIV of a single cylinder. To validate the accuracy of the proposed FSI approach, comparative data from Ahn¹⁰ and Borazjani et al.¹¹ are included. As depicted in the figure, our results exhibit excellent agreement with these benchmark studies. Key observations reveal distinct regime transitions: 1) $U_R = 3$: The cylinder undergoes low-amplitude periodic oscillations about its axis. 2) U_R transition 3 to 4: A dramatic amplitude escalation occurs as the vortex shedding frequency approaches the structural natural frequency, triggering fluidelastic resonance. 3) U_R range 4 to 7: While maintaining large-amplitude vibrations, gradual amplitude attenuation emerges with increasing U_R . 4) U_R transition 7 to 8: The vortex shedding frequency substantially exceeds the natural frequency, effectively suppressing resonance and restoring small-amplitude cyclic motion. This behavior fundamentally demonstrates the lock-in phenomenon characteristic of VIV systems, where maximum vibration amplitudes occur when the Strouhal frequency synchronizes with the structural frequency.

While the primary objective of this study focuses on validating the accuracy of the proposed moving mesh FSI approach, rather than exhaustively investigating the underlying mechanisms of SJs-based VIV suppression, we strategically select a resonant case $\text{Re} = 150, m^* = 2, c^* = 0.0, U_R = 4.0$ to evaluate the suppression efficacy. In the case of SJs-based VIV suppression, the two most common control parameters are SJs velocity magnitude and SJs actuation frequency. Notably, it is obvious that increasing the SJs velocity can impact the boundary layer more strongly and thus suppress the VIV better, but the variation of the SJs frequency affects the suppression effect in a less obvious way. This motivates our investigation into the intrinsic relationship between SJs actuation frequency and suppression performance, providing critical insights for active flow control optimization. The case of Sjs-based VIV suppression is shown in Fig. 13. The jet is positioned at the quarter-arc length on the leeward side of the cylinder, with the jet orifice fixed at an angle of $\alpha = 45^\circ$. The jet velocity is defined as:

$$\begin{aligned} \mathbf{V}_{sj}^u &= U_{\max} \sin(2\pi f_{sj}(t - t_{sj}) + \phi_u) e^{i\beta}, \\ \mathbf{V}_{sj}^l &= U_{\max} \sin(2\pi f_{sj}(t - t_{sj}) + \phi_l) e^{i(-\beta)}. \end{aligned} \quad (30)$$

The superscript or subscripts u and l denote the upper jet and lower jet, respectively. Here, U_{\max} and f_{sj} represent the

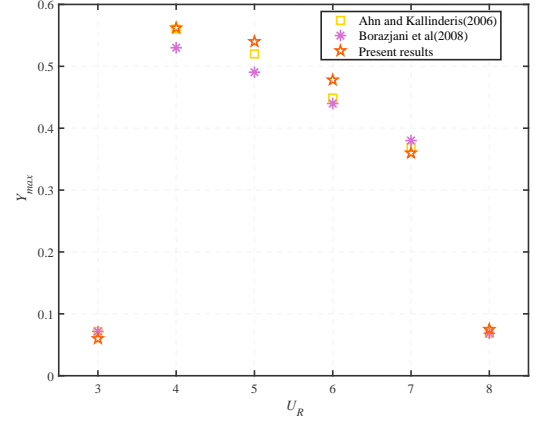


FIG. 12: The maximum dimensionless displacement Y_{\max} computed by IP(3).

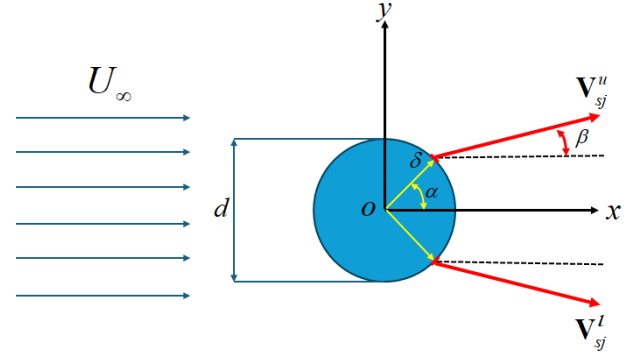


FIG. 13: The sketch of Sjs-based VIV suppression.

maximum jet velocity and jet frequency, t_{sj} specifies the activation time of the jet, and ϕ_u, ϕ_l indicate the phase angles at jet initiation. In this study, these phases are set to $\phi_u = \phi_l = 0$. Additionally, the jet direction is fixed at $\beta = 0^\circ$, corresponding to the horizontal direction. The dimensionless actuation frequency and momentum coefficient of the SJs can be expressed as:

$$f^* = \frac{f_{sj}}{f_v}, C_\mu = \frac{2U_{\max}^2 \delta}{u_\infty^2 d}, \quad (31)$$

where the length of jet orifice is δ , in this study $\delta = \frac{\pi d}{32}$.

Representative cases with dimensionless actuation frequency $f^* = 5, 50, 75, 90$ and momentum coefficient $C_\mu = 3.0$ are investigated to demonstrate the SJs-based VIV suppression efficacy while exploring the frequency-dependent suppression characteristics. To accelerate the cylinder's transition to a steady resonant state, the initial dimensionless displacement is set as $Y(T) = Y(0) = 0.1$. After the VIV reaches a steady state, the jet actuator is activated when the cylinder's displacement transitions from positive to zero. Specifically, the jet is triggered at the dimensionless time: $T_{sj} = \frac{t_{sj}}{d/u_\infty} = 50.0698$ where t_{sj} is the physical jet activation time, d is the cylinder diameter, and u_∞ is the free-stream velocity. The time

evolution of transverse displacement of the cylinder is shown in Fig. 14. The coordinates of points a , b , c , and d for each case in Fig. 14 are listed in Table. III.

Prior to SJs activation, all four cases exhibit identical flow-field evolution patterns. The SJs are synchronously activated at non-dimensional time $T=50.0698$, marked as point J. Post-activation, divergent flowfield developments emerge across cases due to their distinct dimensionless actuation frequencies. As evidenced by the data, cases $a5$, $a50$, $a75$, and $a90$ share identical pre-activation peak displacement coordinates $(T, Y) = (48.9236, 0.562)$. These cases maintain completely congruent flowfield configurations at this critical instant, hereafter collectively designated as reference state "a". At this transitional phase, two coherent vortex streets are observed downstream of the cylinder. Fig. 15 correspondingly presents the non-dimensional vorticity ω_z^* and non-dimensional density ρ^* (where $\rho^* = \frac{\rho}{\rho_\infty}$) contour plots characterizing state "a".

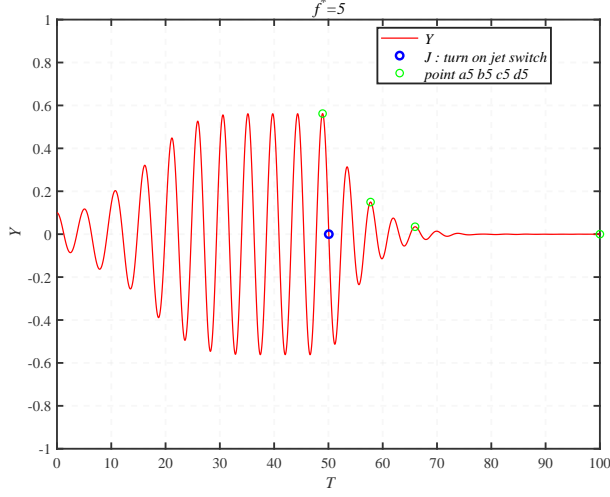
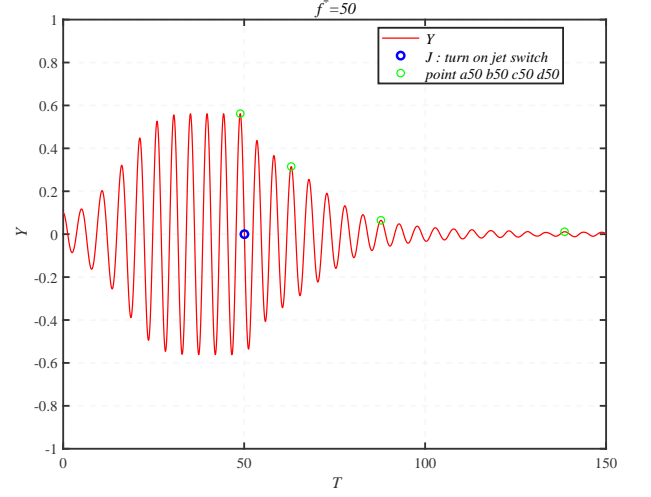
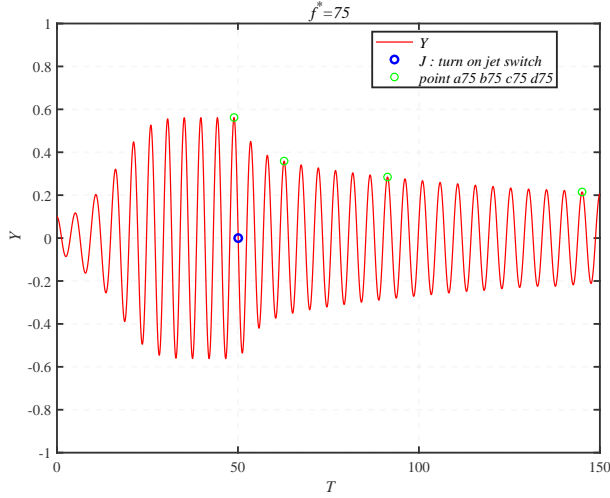
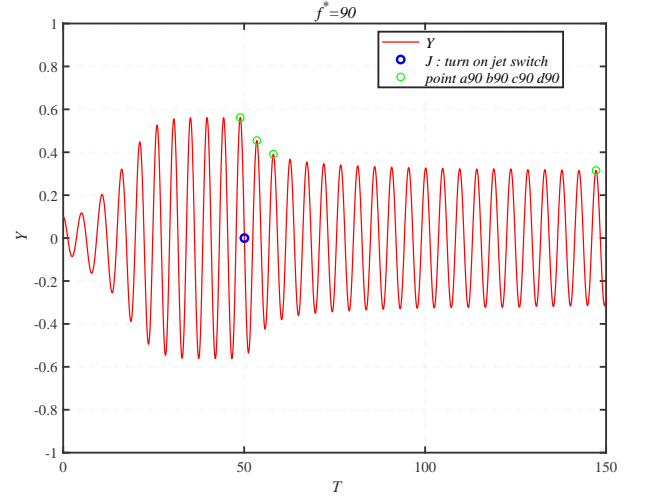
Under the case of $f^*=5$, Fig. 15(a) demonstrates that SJs induces rapid attenuation in the dimensionless displacement amplitude Y of the cylinder with increasing dimensionless time T . Within two oscillation cycles after passing point $a5$, the cylinder reaches point $b5$ at $T=57.7611$, exhibiting a significantly reduced displacement amplitude $Y_{b5} = 0.1497$. This amplitude represents approximately one-fourth of the Y_a , attributed to SJs-induced boundary layer impact which elongates the shedding vortices and initiates their fragmentation. Subsequent evolution reveals further amplitude reduction to $Y_{c5}=0.0346$ at point $c5$ ($T=65.9610$), accompanied by progressively stretched and disintegrated wake vortices. When T exceeds 80 (point $d5$), the Y stabilizes near zero with minimal fluctuations, indicating complete VIV suppression through SJs control. This stabilization corresponds to the establishment of a symmetric flow field maintained by sustained SJs momentum injection. The corresponding vortex dynamics evolution is quantitatively illustrated through dimensionless vorticity ω_z^* and dimensionless density ρ^* contours at characteristic points $b5$, $c5$, and $d5$ in Fig. 16.

Under the case of $f^*=50$, Fig. 14(b) reveals that SJs induces marked attenuation in the dimensionless displacement amplitude Y of the cylinder with increasing dimensionless time T , though the attenuation rate is comparatively slower than observed at $f^*=5$. At characteristic point $d50$ ($Y_{d50}=0.0113$), the VIV is effectively suppressed, achieving near-complete stabilization. The evolutionary characteristics of flow structures are systematically documented through dimensionless vorticity ω_z^* and dimensionless density ρ^* contours at characteristic point $b50$, $c50$, and $d50$ in Fig. 17. The vorticity dynamics captured in Fig. 17 demonstrate elongated attached vortices along cylinder two sides that maintain structural integrity without fragmentation tendencies. Corresponding density field analysis identifies a dual energy transfer mechanism: partial SJs energy propagates as acoustic waves while the remainder directly impacts boundary layer modulation.

Under the case $f^*=75$, Fig. 14(c) demonstrates that following SJs activation, the amplitude of the cylinder's dimensionless displacement Y exhibits slow attenuation with increasing dimensionless time T . At the point $d75$, the amplitude diminishes to $Y_{d75} = 0.2149$ with a decay rate approaching zero, indicating the SJs's insufficient capacity to completely suppress VIV. The evolutionary characteristics of flow structures are systematically documented through dimensionless vortic-

TABLE III: The coordinates of points a , b , c , and d .

	a5	b5	c5	d5
(T, Y)	(48. 9236, 0. 562)	(57. 7611, 0. 1497)	(65. 9610, 0. 0346)	(100, 0. 0001)
	a50	b50	c50	d50
	(48. 9236, 0. 562)	(63. 0031, 0. 3152)	(87. 7822, 0. 0646)	(138. 5217, 0. 0113)
	a75	b75	c75	d75
	(48. 9236, 0. 562)	(62. 7653, 0. 3589)	(91. 3238, 0. 2846)	(145. 0911, 0. 2149)
	a90	b90	c90	d90
	(48. 9236, 0. 562)	(53. 4984, 0. 4545)	(58. 0690, 0. 3914)	(147. 2236, 0. 3153)

(a) $f^* = 5$ (b) $f^* = 50$ (c) $f^* = 75$ (d) $f^* = 90$ FIG. 14: The time evolution of transverse displacement of the cylinder with $f^* = 5, 50, 75, 90$.

ity ω_z^* and dimensionless density ρ^* contours at characteristic point $b75$, $c75$, and $d75$ in Fig. 18. The ω_z^* vorticity contours in Fig. 18 reveal marginally elongated vortices shedding from both sides of the cylinder, while two coherent vortex streets remain observable in the wake region. Comparative analy-

sis of ρ^* contours shows acoustic waves with notably shorter wavelengths than those observed in the $f^*=50$ case. This wavelength reduction enhanced energy's propagation through acoustic wave, where the majority of SJs energy radiates as acoustic waves while only a minor portion is utilized to im-

compact the boundary layer for vibration suppression.

Under the case $f^*=90$, Fig. 14(d) illustrates that SJs activation induces a very slow attenuation of the dimensionless displacement Y amplitude within four oscillation cycles. Beyond this initial phase, the decay rate approaches negligible levels, indicating amplitude stabilization at $Y_{d90} = 0.3153$. This behavior demonstrates further diminished efficacy in VIV suppression compared to lower-frequency cases. The ω_z^* and ρ^* contour distributions at characteristic points $b90$, $c90$, and $d90$ are systematically presented in Fig. 19. Analysis of the ω_z^* vorticity fields reveals that despite high-frequency SJs impingement, shed vortices along the cylinder sides exhibit no significant elongation or fragmentation, with two persistent coherent vortex streets maintained in the wake region. Comparative evaluation of ρ^* contours demonstrates continued wavelength reduction in acoustic waves relative to the $f^*=75$ case. This phenomenon suggests predominant energy dissipation through acoustic radiation, where most of SJs energy propagates as acoustic waves while only a minimal portion is allocated to impact boundary layer for vibration mitigation.

These SJs-controlled VIV suppression cases demonstrate that SJs serves as an efficient and robust solution for vibration mitigation. Furthermore, the results reveal that SJs can achieve completely VIV suppression at a low actuation frequency. However, suppression efficiency decreases at elevated actuation frequencies due to the predominant conversion of SJs energy into acoustic waves rather than effective flow control - a finding consistent with the conclusions drawn by Wang et al.⁵⁴ in their 2016 study. Finally, these cases reconfirm the computational accuracy of the moving mesh FSI approach developed under the RKDG AMR framework presented in this work.

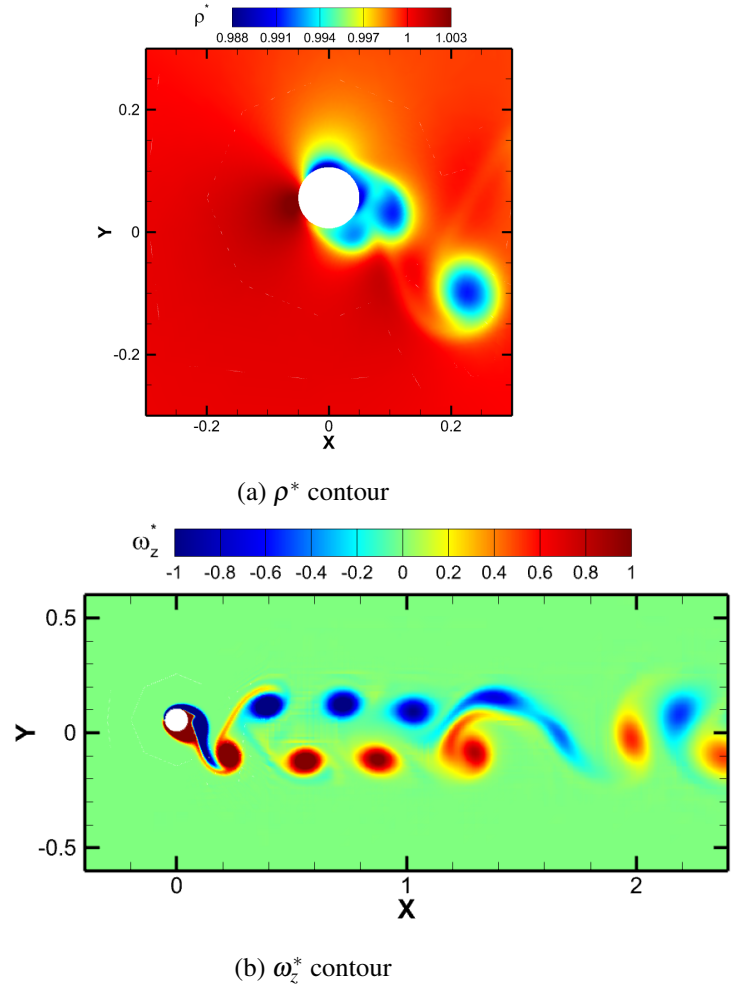
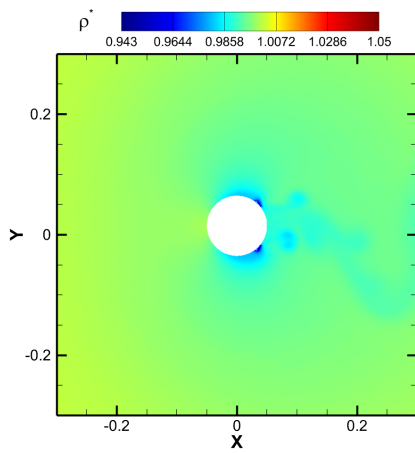
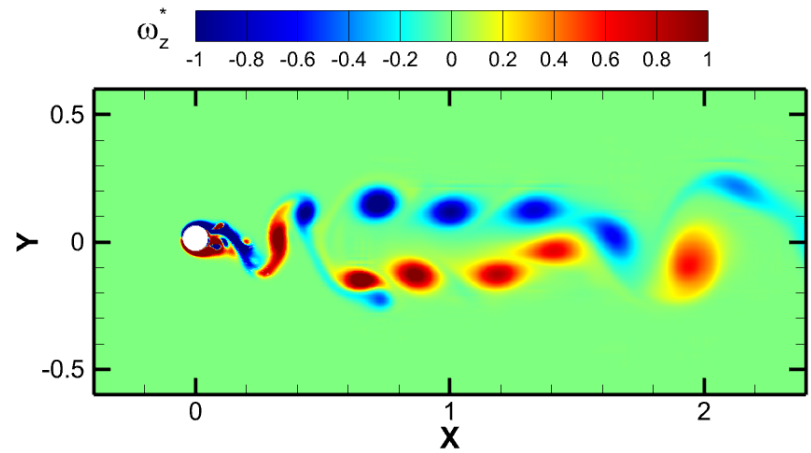
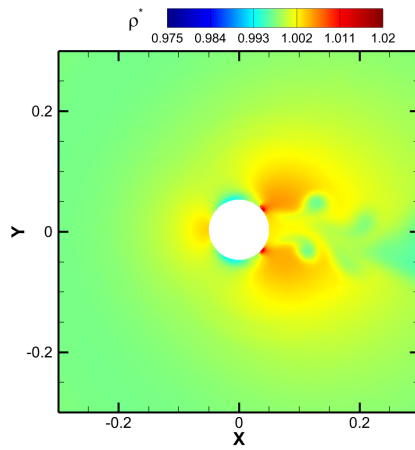
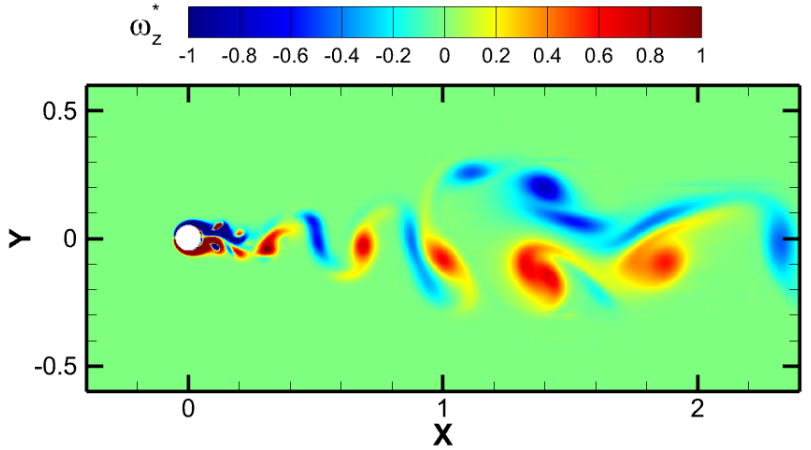
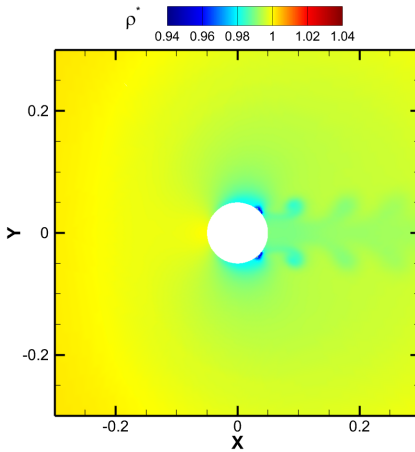
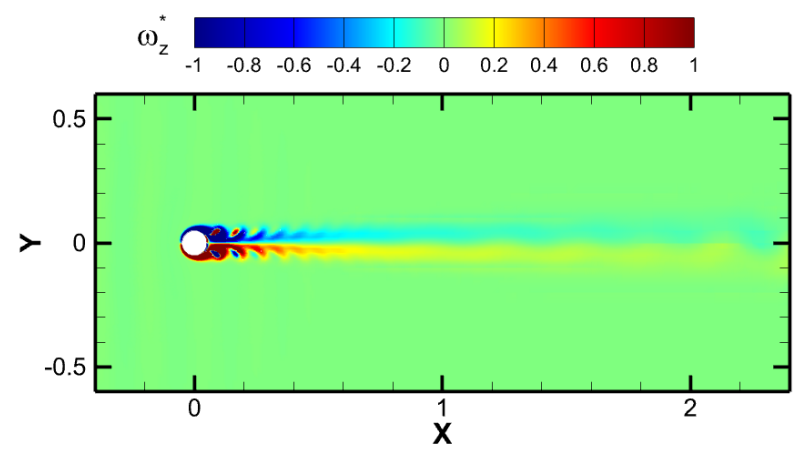
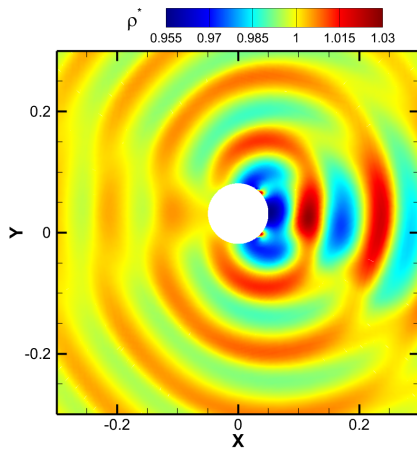
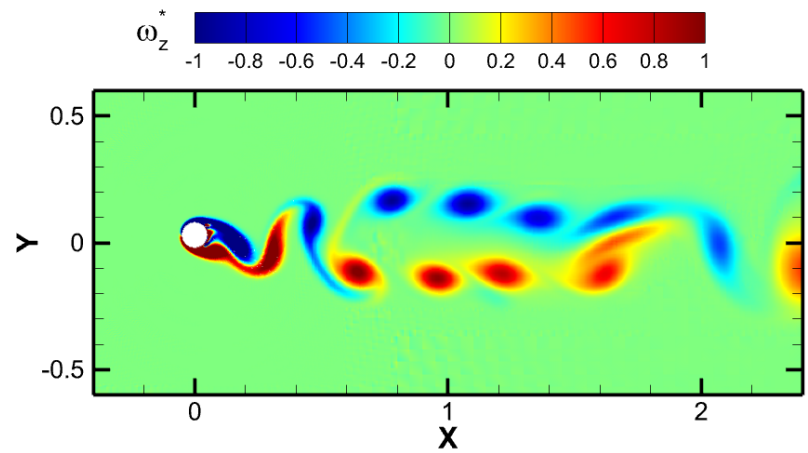
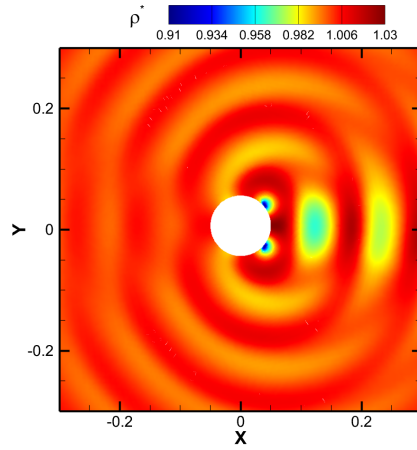
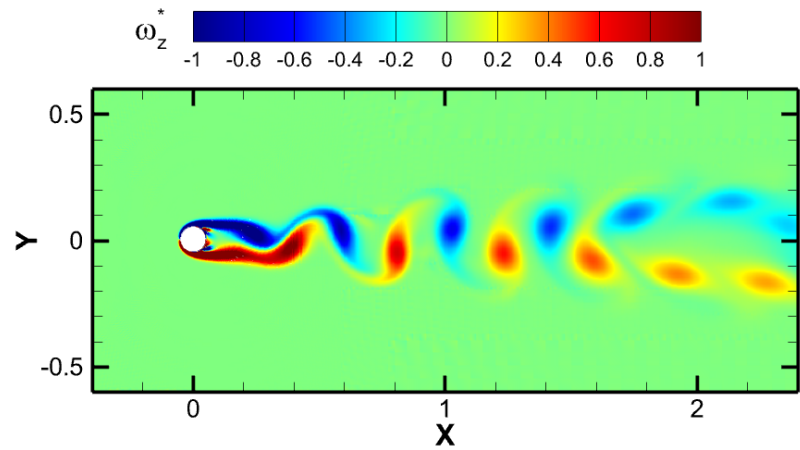
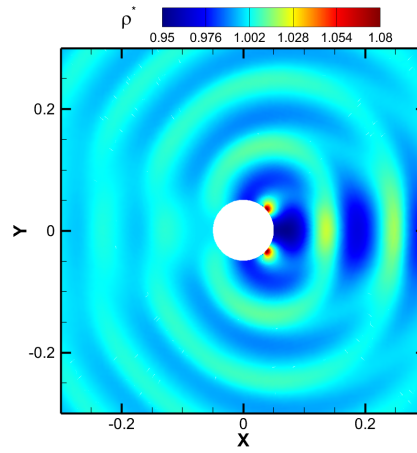
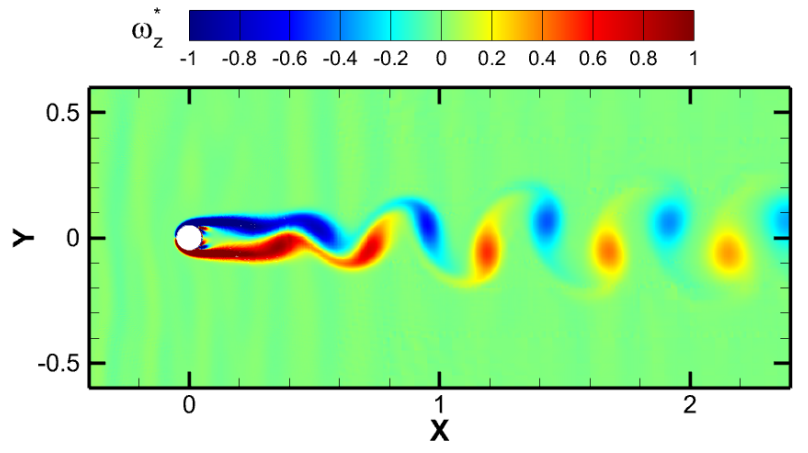
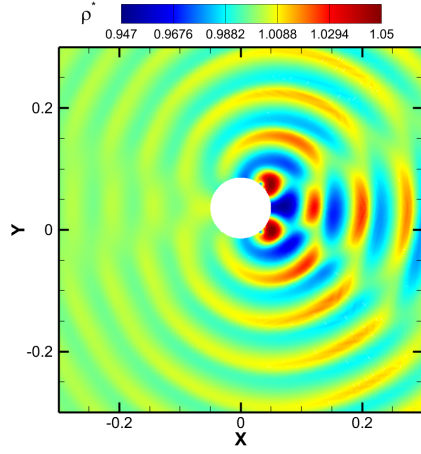


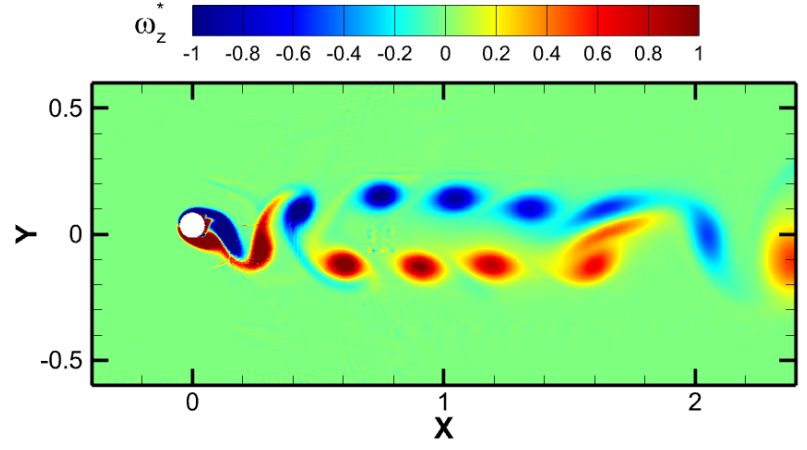
FIG. 15: ω_z^* and ρ^* contour plots at point a

(a) ρ^* contour at points $b5$ (b) ω_z^* contour at points $b5$ (c) ρ^* contour at points $c5$ (d) ω_z^* contour at points $c5$ (e) ρ^* contour at points $d5$ (f) ω_z^* contour at points $d5$ FIG. 16: ω_z^* and ρ^* contour plots at points $b5$, $c5$, and $d5$

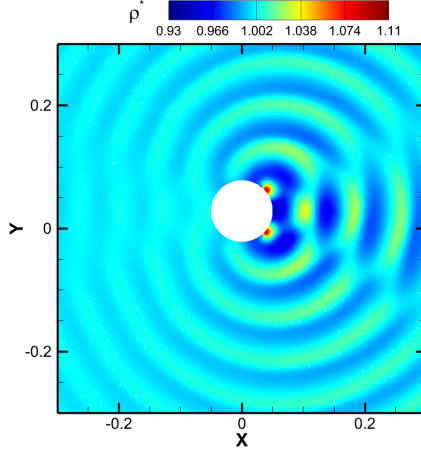
(a) ρ^* contour at points $b50$ (b) ω_z^* contour at points $b50$ (c) ρ^* contour at points $c50$ (d) ω_z^* contour at points $c50$ (e) ρ^* contour at points $d50$ (f) ω_z^* contour at points $d50$ FIG. 17: ω_z^* and ρ^* contour plots at points $b50$, $c50$, and $d50$



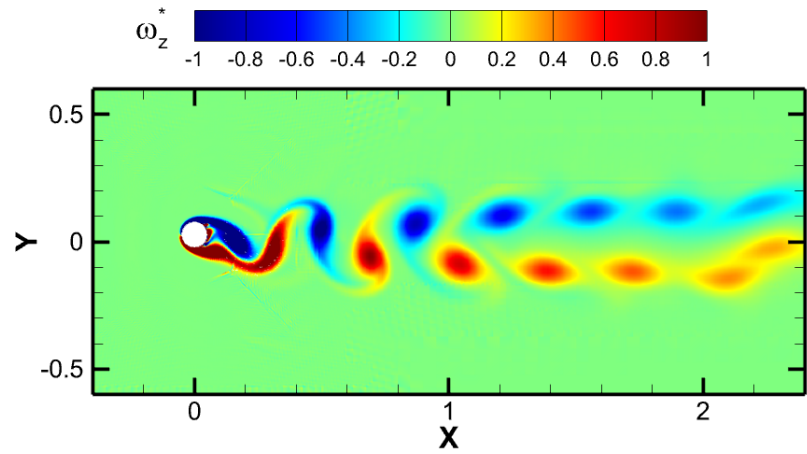
(a) ρ^* contour at points *b75*



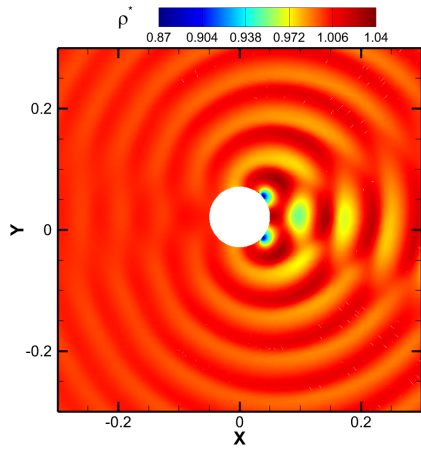
(b) ω_z^* contour at points *b75*



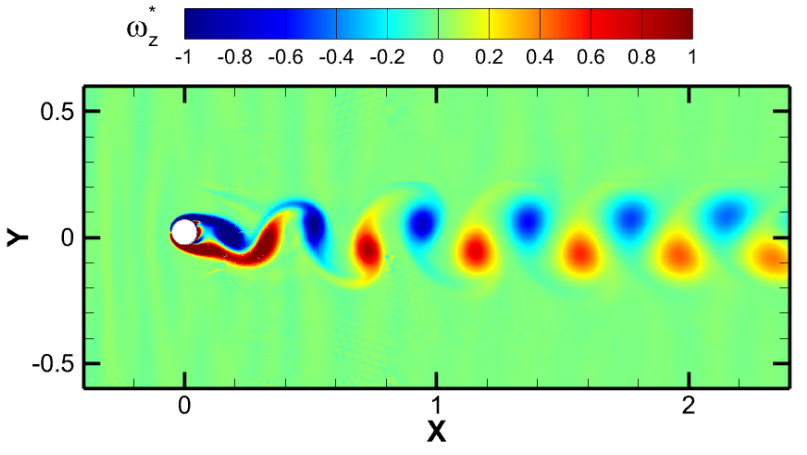
(c) ρ^* contour at points *c75*



(d) ω_z^* contour at points *c75*

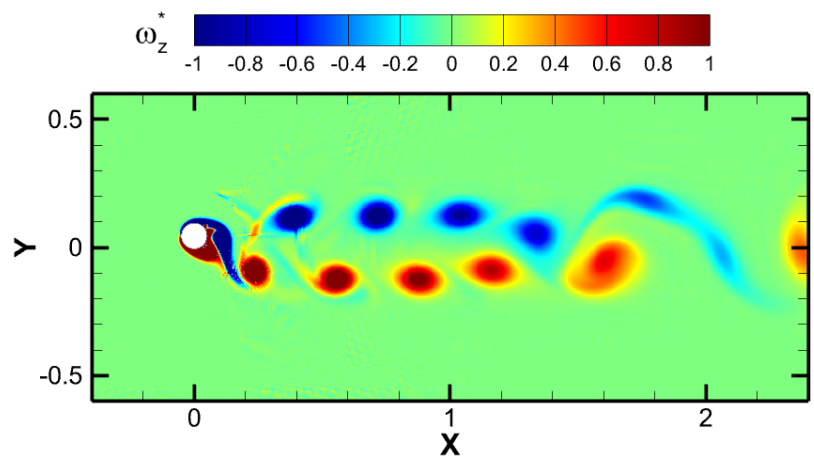
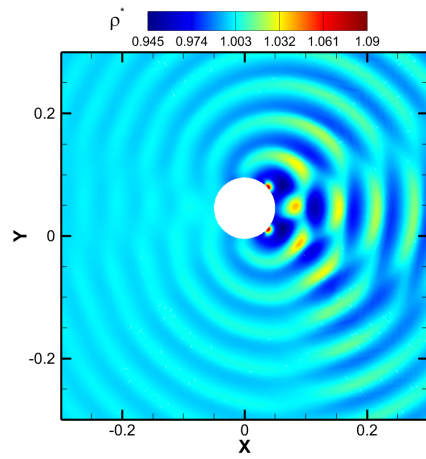
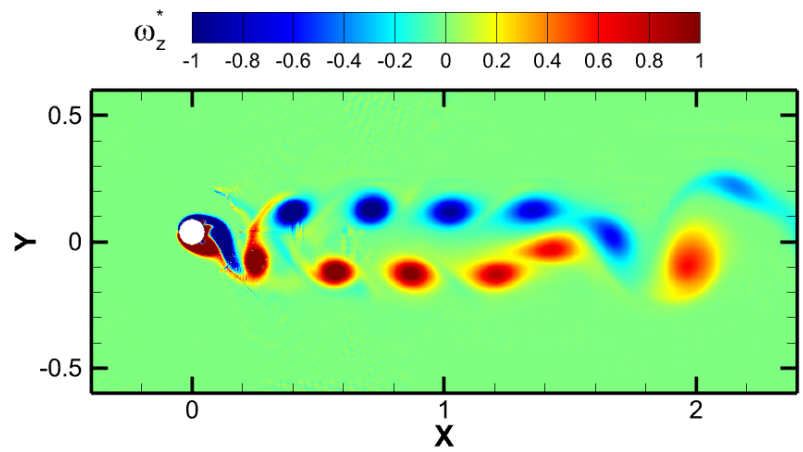
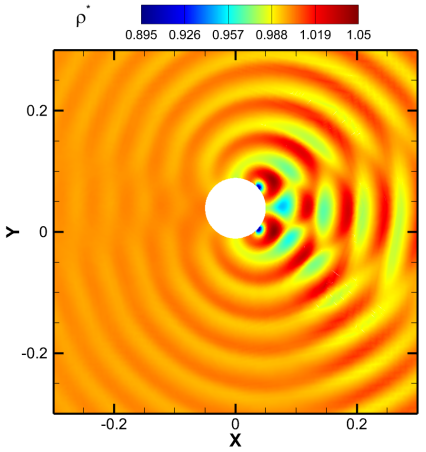
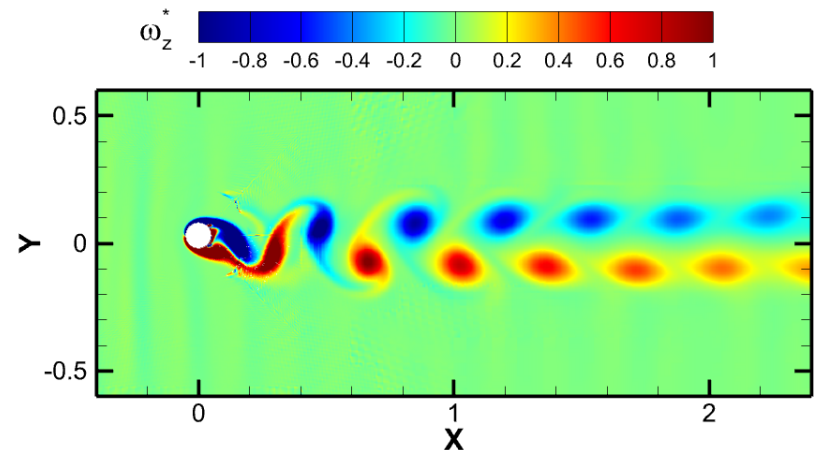
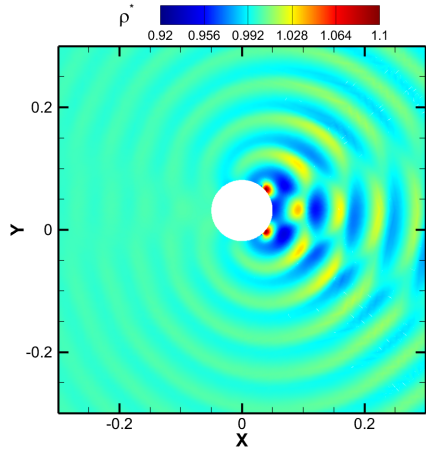


(e) ρ^* contour at points *d75*



(f) ω_z^* contour at points *d75*

FIG. 18: ω_z^* and ρ^* contour plots at points *b75*, *c75*, and *d75*

(a) ρ^* contour at points $b90$ (b) ω_z^* contour at points $b90$ (c) ρ^* contour at points $c90$ (d) ω_z^* contour at points $c90$ (e) ρ^* contour at points $d90$ (f) ω_z^* contour at points $d90$ FIG. 19: ω_z^* and ρ^* contour plots at points $b90$, $c90$, and $d90$

IV. CONCLUSION

In this paper, a moving mesh FSI approach is developed within the RKDG AMR framework. The viscous term in the compressible NS equations is discretized using the high-order IPDG method. Key numerical advancements encompass the rigorous derivation of the Lax-Friedrichs numerical flux formulation tailored for moving meshes, an enhanced AMR-driven nodal correction methodology designed for curved surface geometries, and the implementation of a ghost-node boundary condition treatment scheme to address dynamic mesh motion. In Couette flow simulation, the IPDG method demonstrated its high-order accuracy characteristics. In the simulation of unsteady flow past a cylinder, the AMR technology demonstrated its capability to maintain high resolution while reducing computational costs. The six VIV benchmark cases validated the accuracy of the moving mesh approach. Furthermore, the proposed moving mesh FSI approach was applied to investigate the VIV suppression of a single cylinder under active flow control. The results demonstrated that SJs can effectively suppress VIV at a low actuation frequency, while higher actuation frequencies lead to reduced suppression efficiency due to the energy of the SJs is more in the form of acoustic wave. The following conclusions are obtained:

1. The RKDG AMR framework demonstrates superior numerical stability and high-order accuracy characteristics, where the AMR technology effectively optimizes computational resource allocation while preserving solution fidelity.

2. The IPDG algorithm exhibits significant computational advantages in hydrodynamic simulations through its inherent high-order spatial resolution capabilities.

3. The moving mesh FSI approach developed within the RKDG AMR framework has exceptional performance in VIV simulations.

4. SJs is an efficient and robust solution for vibration mitigation, SJs can achieve completely VIV suppression at a low actuation frequency, while higher actuation frequencies reduce suppression efficiency due to the energy of the SJs is more in the form of acoustic wave.

ACKNOWLEDGMENTS

DATA AVAILABILITY

The data that support the findings of this study are available within the article.

REFERENCES

- ¹W. Xu, K. Jia, Y. Ma, Y. Wang, and Z. Song, "Multispan classification methods and interaction mechanism of submarine pipelines undergoing vortex-induced vibration," *Applied Ocean Research* **120**, 103027 (2022).
- ²T. Zhang, S. Zhang, D. Yang, and G. Huang, "Numerical investigation on competitive mechanism between internal and external effects of submarine pipeline undergoing vortex-induced vibration," *Ocean Engineering* **266**, 112744 (2022).
- ³Y. Lu, Z. Liu, W. Xu, and Y. Ma, "Vortex-induced vibration (viv) fatigue damage characteristics of submarine multispan pipelines," *Ocean Engineering* **324**, 120666 (2025).
- ⁴A. Suleman and P. Moniz, "Active aeroelastic aircraft structures," in *Computational Mechanics* (Springer, 2006) pp. 85–106.
- ⁵M. d. C. Henshaw, K. J. Badcock, G. Vio, C. Allen, J. Chamberlain, I. Kaynes, G. Dimitriadis, J. Cooper, M. Woodgate, A. M. Rampurawala, *et al.*, "Non-linear aeroelastic prediction for aircraft applications," *Progress in Aerospace Sciences* **43**, 65–137 (2007).
- ⁶H. Chen, K. Xia, H. Deng, M. Zhu, and J. Teng, "Investigation of aeroelastic instability in a transonic compressor with low engine order distortion," *Aerospace Science and Technology* **159**, 109953 (2025).
- ⁷S. Chen and C. Cai, "Evolution of long-span bridge response to wind-numerical simulation and discussion," *Computers & structures* **81**, 2055–2066 (2003).
- ⁸C. Cai and S. Chen, "Wind vibration mitigation of long-span bridges in hurricanes," *Journal of sound and vibration* **274**, 421–432 (2004).
- ⁹Y. Zhang, P. Cardiff, and J. Keenahan, "Wind-induced phenomena in long-span cable-supported bridges: a comparative review of wind tunnel tests and computational fluid dynamics modelling," *Applied Sciences* **11**, 1642 (2021).
- ¹⁰H. T. Ahn and Y. Kallinderis, "Strongly coupled flow/structure interactions with a geometrically conservative ale scheme on general hybrid meshes," *Journal of Computational Physics* **219**, 671–696 (2006).
- ¹¹I. Borazjani, L. Ge, and F. Sotiropoulos, "Curvilinear immersed boundary method for simulating fluid structure interaction with complex 3d rigid bodies," *Journal of Computational physics* **227**, 7587–7620 (2008).
- ¹²H. T. Ahn and Y. Kallinderis, "Strongly coupled flow/structure interactions with a geometrically conservative ale scheme on general hybrid meshes," *Journal of Computational Physics* **219**, 671–696 (2006).
- ¹³F. Xie, J. Deng, Q. Xiao, and Y. Zheng, "A numerical simulation of viv on a flexible circular cylinder," *Fluid Dynamics Research* **44**, 045508 (2012).
- ¹⁴H. Jiao, *Vortex-Induced Vibration of Circular Cylinders Using Multi-Block Immersed Boundary-Lattice Boltzmann Method*, Ph.D. thesis, UCL (University College London) (2021).
- ¹⁵B. Cockburn and C.-W. Shu, "Runge-kutta discontinuous galerkin methods for convection-dominated problems," *Journal of scientific computing* **16**, 173–261 (2001).
- ¹⁶J. Liu, J. Qiu, M. Goman, X. Li, and M. Liu, "Positivity-preserving runge-kutta discontinuous galerkin method on adaptive cartesian grid for strong moving shock," *Numerical Mathematics: Theory, Methods and Applications* **9**, 87–110 (2016).
- ¹⁷J. Zhu, X. Zhong, C.-W. Shu, and J. Qiu, "Runge-kutta discontinuous galerkin method using a new type of weno limiters on unstructured meshes," *Journal of Computational Physics* **248**, 200–220 (2013).
- ¹⁸F. Bassi and S. Rebay, "A high-order accurate discontinuous finite element method for the numerical solution of the compressible navier-stokes equations," *Journal of computational physics* **131**, 267–279 (1997).
- ¹⁹J. Manzanero, A. M. Rueda-Ramírez, G. Rubio, and E. Ferrer, "The bassi rebay I scheme is a special case of the symmetric interior penalty formulation for discontinuous galerkin discretisations with gauss-lobatto points," *Journal of Computational Physics* **363**, 1–10 (2018).
- ²⁰S. Bosnyakov, S. Mikhaylov, V. Y. Podaruev, and A. Troshin, "Unsteady discontinuous galerkin method of a high order of accuracy for modeling turbulent flows," *Mathematical Models and Computer Simulations* **11**, 22–34 (2019).
- ²¹D. N. Arnold, F. Brezzi, B. Cockburn, and L. D. Marini, "Unified analysis of discontinuous galerkin methods for elliptic problems," *SIAM journal on numerical analysis* **39**, 1749–1779 (2002).

- ²²D. N. Arnold, “An interior penalty finite element method with discontinuous elements,” *SIAM journal on numerical analysis* **19**, 742–760 (1982).
- ²³R. Hartmann and P. Houston, “An optimal order interior penalty discontinuous galerkin discretization of the compressible navier–stokes equations,” *Journal of Computational Physics* **227**, 9670–9685 (2008).
- ²⁴F. Heimann, C. Engwer, O. Ippisch, and P. Bastian, “An unfitted interior penalty discontinuous galerkin method for incompressible navier–stokes two-phase flow,” *International Journal for Numerical Methods in Fluids* **71**, 269–293 (2013).
- ²⁵M. Kaltenbach, “A local discontinuous galerkin approximation for the p-navier–stokes system, part i: convergence analysis,” *SIAM Journal on Numerical Analysis* **61**, 1613–1640 (2023).
- ²⁶M. Baccouch, “A local discontinuous galerkin method for the second-order wave equation,” *Computer Methods in Applied Mechanics and Engineering* **209**, 129–143 (2012).
- ²⁷B. Cockburn and C.-W. Shu, “The local discontinuous galerkin method for time-dependent convection-diffusion systems,” *SIAM journal on numerical analysis* **35**, 2440–2463 (1998).
- ²⁸J. Peraire and P.-O. Persson, “The compact discontinuous galerkin (cdg) method for elliptic problems,” *SIAM Journal on Scientific Computing* **30**, 1806–1824 (2008).
- ²⁹S. Brdar, A. Dedner, and R. Klöforn, “Compact and stable discontinuous galerkin methods for convection-diffusion problems,” *SIAM Journal on Scientific Computing* **34**, A263–A282 (2012).
- ³⁰J. Cheng, X. Yang, X. Liu, T. Liu, and H. Luo, “A direct discontinuous galerkin method for the compressible navier–stokes equations on arbitrary grids,” *Journal of Computational Physics* **327**, 484–502 (2016).
- ³¹F. Zhang, J. Cheng, and T. Liu, “A direct discontinuous galerkin method for the incompressible navier–stokes equations on arbitrary grids,” *Journal of Computational Physics* **380**, 269–294 (2019).
- ³²H. Liu and J. Yan, “The direct discontinuous galerkin (ddg) methods for diffusion problems,” *SIAM Journal on Numerical Analysis* **47**, 675–698 (2009).
- ³³K. Schaal, A. Bauer, P. Chandrashekar, R. Pakmor, C. Klingenberg, and V. Springel, “Astrophysical hydrodynamics with a high-order discontinuous galerkin scheme and adaptive mesh refinement,” *Monthly Notices of the Royal Astronomical Society* **453**, 4278–4300 (2015).
- ³⁴A. Papoutsakis, S. S. Sazhin, S. Begg, I. Danaila, and F. Luddens, “An efficient adaptive mesh refinement (amr) algorithm for the discontinuous galerkin method: Applications for the computation of compressible two-phase flows,” *Journal of Computational Physics* **363**, 399–427 (2018).
- ³⁵L. Wang and D. J. Mavriplis, “Adjoint-based h–p adaptive discontinuous galerkin methods for the 2d compressible euler equations,” *Journal of Computational Physics* **228**, 7643–7661 (2009).
- ³⁶Y.-L. Liu, A.-M. Zhang, Q. Kong, L. Chena, Q. Haoa, and Y. Cao, “An unstructured block-based adaptive mesh refinement approach for explicit discontinuous galerkin method,” (2025), arXiv:2502.12620 [physics.flu-dyn].
- ³⁷E. F. Toro, *Riemann solvers and numerical methods for fluid dynamics: a practical introduction* (Springer Science & Business Media, 2013).
- ³⁸A. Glezer and M. Amitay, “Synthetic jets,” *Annual review of fluid mechanics* **34**, 503–529 (2002).
- ³⁹M. Ivings, D. Causon, and E. F. Toro, “On riemann solvers for compressible liquids,” *International Journal for Numerical Methods in Fluids* **28**, 395–418 (1998).
- ⁴⁰S. Gottlieb, C.-W. Shu, and E. Tadmor, “Strong stability-preserving high-order time discretization methods,” *SIAM review* **43**, 89–112 (2001).
- ⁴¹R. Hartmann, “Adaptive discontinuous galerkin methods with shock-capturing for the compressible navier–stokes equations,” *International Journal for Numerical Methods in Fluids* **51**, 1131–1156 (2006).
- ⁴²Y. Liu, W. Guo, Y. Jiang, and M. Zhang, “Non-oscillatory entropy stable dg schemes for hyperbolic conservation law,” arXiv preprint arXiv:2410.16729 (2024).
- ⁴³H. Luo, “A reconstructed discontinuous galerkin method based on a hierarchical weno reconstruction for computing shock waves on hybrid grids,” in *21st AIAA Computational Fluid Dynamics Conference* (2013) p. 3063.
- ⁴⁴R. Hartmann and P. Houston, “Symmetric interior penalty dg methods for the compressible navier–stokes equations ii: Goal-oriented a posteriori error estimation,” *International Journal of Numerical Analysis & Modeling* **3**, 141–162 (2006).
- ⁴⁵L. Yunlong, W. Pingping, W. Shipping, and Z. Aman, “Numerical analysis of transient fluid-structure interaction of warship impact damage caused by underwater explosion using the fslab,” *Chinese Journal of Ship Research* **17**, 228–240 (2022).
- ⁴⁶Q. Kong, Y.-L. Liu, S. Ma, and A. Zhang, “Numerical simulation of supersonic sea-skimming flight based on discontinuous galerkin method with adaptive mesh refinement framework,” *Physics of Fluids* **35** (2023).
- ⁴⁷K. W. Schulz and Y. Kallinderis, “Unsteady flow structure interaction for incompressible flows using deformable hybrid grids,” *Journal of Computational Physics* **143**, 569–597 (1998).
- ⁴⁸Y. Sun, Z. J. Wang, and Y. Liu, “High-order multidomain spectral difference method for the navier–stokes equations,” in *44th AIAA Aerospace Sciences Meeting and Exhibit* (2007) p. 301.
- ⁴⁹B. Engquist and A. Majda, “Absorbing boundary conditions for the numerical simulation of waves,” *Mathematics of computation* **31**, 629–651 (1977).
- ⁵⁰L. Zhang, W. Liu, M. Li, X. He, and H. Zhang, “A class of dg/fv hybrid schemes for conservation law iv: 2d viscous flows and implicit algorithm for steady cases,” *Computers & Fluids* **97**, 110–125 (2014).
- ⁵¹B. Müller, “High order numerical simulation of aeolian tones,” *Computers & Fluids* **37**, 450–462 (2008).
- ⁵²J. Wang, X. Shi, Q. Zhang, and J. Chang, “Effect of synthetic jet on naca0012 airfoil vortex structure and aerodynamic characteristics,” *Journal of Applied Fluid Mechanics* **17**, 1052–1072 (2024).
- ⁵³H. Wang, P. Zhang, H. Yu, Q. Zou, and Y. Sun, “Numerical investigation of synthetic jet effects on vortex-induced vibrations in tandem circular cylinders,” *Ships and Offshore Structures* , 1–13 (2024).
- ⁵⁴C. Wang, H. Tang, F. Duan, and C. Simon, “Control of wakes and vortex-induced vibrations of a single circular cylinder using synthetic jets,” *Journal of Fluids and Structures* **60**, 160–179 (2016).